

This work is on a Creative Commons Attribution-NonCommercial-NoDerivatives 4.0 International (CC BY-NC-ND 4.0) license, <https://creativecommons.org/licenses/by-nc-nd/4.0/>. Access to this work was provided by the University of Maryland, Baltimore County (UMBC) ScholarWorks@UMBC digital repository on the Maryland Shared Open Access (MD-SOAR) platform.

Please provide feedback

Please support the ScholarWorks@UMBC repository by emailing scholarworks-group@umbc.edu and telling us what having access to this work means to you and why it's important to you. Thank you.

***Modeling Molten Droplet Spreading and Infiltration into Non-Isothermal
Thermal Barrier Coatings***

Timothy Munuhe, Ruey-Hung Chen, Liang Zhu, Ronghui Ma

Department of Mechanical Engineering

University of Maryland, Baltimore County

1000 Hilltop Circle, Baltimore, MD 21250

Abstract

Molten calcium-magnesium-alumino-silicate (CMAS) droplets impact and infiltrate porous thermal barrier coatings (TBCs) of gas turbines, thereby causing loss of strain tolerance and delamination of the ceramic topcoat. To develop efficient mitigation strategies, it is crucial to understand CMAS infiltration dynamics into the porous topcoat. An integrated model is introduced incorporating simultaneous droplet spreading, wetting interactions, heat transfer, and liquid infiltration with temperature-dependent viscosities in unsaturated porous media. The model is applied to CMAS droplet interactions with homogeneous/heterogeneous anisotropic TBC topcoats grown by the electron beam physical vapor deposition (EB-PVD) method. Simulation results show that the droplet height and contact diameter dynamics exhibit three stages - initial-stage fast decrease, slow quasi-linear intermediate decrease, and late-stage fast decrease. The first two stages are dominated by the dynamics of infiltration. The initial temperature of the droplet has insignificant effect on the infiltration dynamics. Rather, the temperature gradient in the topcoat is critical to the infiltration rate. The anisotropy determines the final infiltration diameter and depth. Further, bilayer and multilayer coating structures with alternating fine and coarse columns can delay the infiltration rate and promote lateral spreading during the early stage of the droplet infiltration compared to single-layer structures. The results demonstrate that heterogeneous structures provide a viable approach to mitigate fast infiltration and reduce damage to the TBCs during the early stage of droplet infiltration.

Keywords: droplet spreading, droplet infiltration in anisotropic porous medium, CMAS, temperature-dependent viscosity, thermal barrier coatings

Nomenclature

A, B, C	=	constants for viscosity model	<i>Subscripts</i>	
c	=	color function	b	= bottom
c_p	=	specific heat capacity (J/(kg·K))	c	= capillary, or contact
D	=	characteristic length of columns (m)	d	= droplet
dt	=	time step (s)	e	= equilibrium
h	=	droplet height (m)	eff	= effective
h^*	=	film thickness (m)	l	= liquid
h_p	=	infiltration depth (m)	i	= inner dimension
g	=	gravitational acceleration (m/s ²)	o	= outer dimension
k	=	thermal conductivity (W/(m·K))	p	= porous medium
K	=	hydraulic permeability (m ²)	top	= at the top surface, where $z = 0$
H	=	topcoat thickness (m)	0	= at initial time
L	=	maximum domain length (m)		
\vec{n}	=	unit vector		
P	=	pressure (Pa)		
R_c	=	contact radius (m)		
R_w	=	wetted radius (m)		
r	=	radius (m)		
T	=	temperature (°C)		
u, w	=	velocity (m/s)		
z	=	position (m)		
ε	=	porous medium porosity		
θ	=	contact angle (°)		
μ	=	viscosity (Pa·s)		
ρ	=	density (kg/m ³)		
σ	=	surface tension (Pa·m)		
τ	=	tortuosity		
γ	=	surface curvature (m ⁻¹)		

1. Introduction

An efficient approach to enhance the fuel performance of gas turbines is to increase the inlet gas temperature. To achieve this goal, thermal barrier coatings (TBCs) are used to protect the turbine blade. Typical TBCs have a multilayer structure with a porous topcoat, commonly made from 7 wt.% yttria-stabilized zirconia (7YSZ), grown on a metallic bond coat and superalloy substrate. The 7YSZ topcoat offers combined thermal insulation and strain tolerance in a high temperature environment. When operating in dusty environments such as deserts, near volcanic eruptions, and highly polluted areas [1-3], aero-gas turbine engines may breathe in siliceous particles that can melt in the internal hot gas stream [4-6]. The molten silicate materials produced from sand, dust, and volcanic ash, are generally referred to as CMAS (calcium-magnesium-alumino-silicate). These molten particles may impact and adhere to the TBCs, eventually infiltrating into the porous topcoat. The molten CMAS may react directly with the TBC constituents and cause destabilization of the topcoat, accelerated oxidation and hot corrosion of the underlying metallic bond coat and superalloy substrate [7-9]. Upon cooling, the infiltrated CMAS stiffens the topcoat, and the loss in strain and stress tolerance causes delamination of the coated material. These CMAS-associated thermo-chemical and thermo-mechanical damages ultimately accelerate the failure of TBCs and underlying components. Thereby, CMAS droplet interactions with TBCs have attracted renewed interest in recent years [10-12].

Although spreading, splash, rebounding, and surface tension-induced oscillation can occur for droplet impact at high speeds [13], fully molten CMAS is very viscous and wets 7YSZ topcoats well, such that droplet rebound/oscillation has not been observed [10-12]. The infiltration of a CMAS droplet into the pores of the TBC topcoat is mainly driven by the capillary pressure at the infiltration front, characterized by strong wetting interactions between a highly viscous liquid and a low-porosity medium under a large temperature gradient normal to the coating surface. The infiltration rate is governed by multiple factors including the structural characteristics of the topcoat, the temperature distribution in the TBC, as well as the properties of the CMAS such as viscosity, melting point, and wetting on the porous material. Moreover, the droplet may have a higher temperature than the substrate, which may elevate the temperature of the contact area. The coupling of the fluid infiltration and heat transfer through the temperature-dependent CMAS viscosity further adds complexity to understanding the spreading and infiltration process.

Consequently, how the CMAS's and TBC's thermal behavior and interaction affects the spreading and infiltration process has not been well understood.

Currently, two different experimental approaches have been used to investigate CMAS infiltration in TBCs. One approach focuses on a large reservoir of molten CMAS infiltrating into a heated TBC [3, 14-17] without considering the droplet interactions with the topcoat. As such, this approach is mainly used to characterize the TBC topcoat materials with or without a temperature gradient. The other approach is sessile droplet sorption where a single droplet is placed on a substrate, and the evolution of the droplet profile and the equilibrium contact angle are measured [18-23]. Experimental studies have examined molten CMAS spreading on impermeable surfaces [21, 22] and interacting with porous TBCs [9, 18, 23], with special focus on how the CMAS composition, substrate material, substrate surface morphology, and substrate temperature affect spreading. Song et al. [22] found that a large fully molten CMAS droplet's spreading dynamics on an impermeable alumina substrate follow a modified Tanner's law. Multiple studies confirmed that CMAS partially wets 7YSZ topcoats and some suggest that the wetting interactions vary with temperature [24]. Yang et al. [20] highlighted the importance of the temperature-dependent viscosity on the spreading and infiltration processes of a CMAS droplet on a 7YSZ porous substrate in isothermal environments at different temperatures.

As these studies [9, 18, 20-23] focused on wetting behavior, millimeter-sized CMAS droplets were used on the TBC topcoats with hundreds-of-micrometers thicknesses. In fact, the CMAS droplet size in a gas turbine is less than 100 μm , up to an order of magnitude smaller than the topcoat thickness. As a result, the infiltration front of such small droplets does not reach to the bottom of the topcoat before being fully absorbed. Therefore, studies utilizing large droplets do not elucidate the infiltration dynamics of a CMAS droplet in TBCs of a gas turbine. Moreover, experimental studies conducted in isothermal environment do not reveal to what extent the droplet's initial temperature affects the infiltration process, nor the effect of the temperature gradient in a TBC topcoat on the CMAS droplet spreading and infiltration dynamics.

Extensive theoretical studies have been conducted to examine sessile droplet spreading and sorption in rigid porous media [25-28]. An earlier-developed modeling approach assumes that the droplet retains the shape of a spherical cap throughout the sorption process [27, 29, 30] and focuses on the contact line behavior to define the contact area through which the liquid enters the porous

medium. The mass conservation is ensured by adjusting the volume of the droplet above the porous medium. However, this method excludes the effect of droplet spreading dynamics on sorption.

Another modeling approach employs the lubrication approximation and assumes that the droplet is thin and has negligible inertia [26, 27]. Based on these assumptions, the continuity and Navier-Stokes equations are reduced to a transient height profile over a one-dimensional or a two-dimensional space. It has been used to model two- and three-dimensional spreading and infiltration problems [25, 28, 31, 32]. The wetting interactions at the contact line are included by assuming a thin precursor film over the top surface and applying the disjoining pressure in the liquid layer [31 – 34]. Based on the lubrication theory and continuum approximation of the porous medium, Espín & Kumar [31] investigated contact line pinning of droplets on rough, thin, and saturated porous substrates and successfully replicated droplet behaviors observed in experiments [35]. Wang et al. [32] conducted experimental and numerical study of water droplet spreading and imbibition on melt-blown fiber mats with special emphasis on surface wetting modification by hydrolysis and the influence of hydrolysis time on droplet absorption. Ahmed & Sellier [36] researched droplet spreading and infiltration into flat and inclined porous substrates and found power-law relationships between the sorption time and permeability and porosity. Additionally, they found an exponential relationship between the sorption time and equilibrium contact angle. Chen [37] presented a model for Newtonian and non-Newtonian droplet spreading and sorption into a homogeneous porous medium and found that the infiltration front is largely flat under the contact area, similar to findings by Alleborn & Raszillier [25] and Zdražil et al. [28].

Few of the studies of sessile droplet sorption using lubrication theory considered a simultaneous heat transfer and droplet infiltration [28, 38 – 40]. Zdražil et al. [28] investigated axisymmetric hot droplet spreading, infiltration, and solidification into a cold porous substrate but they assumed temperature-independent material properties. A fine mesh was used in this study to capture the temperature gradient and solid/liquid interface in the droplet. Barić & Steiner [38] considered non-isothermal liquid flow through a die with temperature-dependent viscosity. More recently, Dai et al. [39] considered droplet spreading across a heated surface considering thermocapillary migration. Although they acknowledged that faster migration occurs at high temperature due to temperature-dependent liquid viscosity, they did not include such effects in their numerical model. Pham & Kumar [40] considered heat transfer within a droplet in the context of simultaneous

droplet spreading, infiltration, and evaporation. The substrate was isothermal with steady-state temperature.

To enhance resistance to CMAS infiltration, the TBC top layer can be fabricated to possess heterogeneous structures with varying pore microstructures. Such a morphology reduces the infiltration rate by limiting wetting interactions and/or using low-permeability microstructures [41]. To achieve an optimized microstructure, there is a need for better understanding of how heterogeneous microstructures affect CMAS droplet infiltration behavior in porous TBC topcoats. Further, while infiltration is the focus of CMAS investigations, observing it directly is difficult with current technology. Of interest to researchers is if any inferences can be made of the infiltration process given the normally visible droplet height, contact radius, and sometimes observable wetted radius.

In this study, an integrated model is developed incorporating heat transfer and temperature-dependent viscosity as well as simultaneous droplet spreading, wetting, and infiltration in unsaturated isotropic/anisotropic porous structures. Numerical simulations are conducted with this model to obtain quantitative information on the relationship between the infiltration depth and droplet spreading parameters. This model is also used to study the effect of droplet temperature, temperature gradient in the topcoats, and various coating microstructures on CMAS infiltration. It is anticipated that quantitative information and advanced understanding of the spreading and infiltration dynamics would benefit the development of anti-CMAS infiltration solutions.

2. Mathematical Model

Droplet impact and sorption in a porous medium can be divided into two distinct stages: an initial stage in which the droplet experiences impact and fast spreading driven by the droplet's inertia and kinetic energy, followed by a stage dominated by the droplet infiltration in the underlying porous medium. Upon impact, rebounding and oscillation may occur depending on the surface tension and wettability. For CMAS droplets less than 100 μm in diameter, although they impact the surface at a high speed, rebounding and oscillation have not been observed due to the high viscosity and the very good wettability of the TBC [11, 13]. It is generally accepted that the kinetic energy dissipates quickly, and the initial impact and spreading period is on the order of microseconds [42]. Moreover, the viscous CMAS infiltration into the TBC topcoats with porosity less than 20% is a slow process. It is thus reasonable to consider infiltration during the first stage

negligible. In fact, the infiltration dynamics in the second stage determine the rate and depth of the CMAS penetration in the topcoat. Therefore, this study focuses on the second stage where the CMAS droplet sorption is dominated by the capillary pressure acting at the infiltration front rather than the initial impact and fast spreading of the droplet.

The CMAS droplet (with a diameter less than $70 \mu\text{m}$) is small and its spreading and infiltration are assumed to occur over a flat surface. The coating of this study is the 7YSZ topcoat deposited by the electron beam physical vapor deposition (EB-PVD) method. The EB-PVD topcoat has a columnar microstructure that is assumed to have in-plane homogeneity. This simplification allows the problem to be treated as two-dimensional axisymmetric spreading and infiltration considered in the $r - z$ plane. The liquid is assumed incompressible with constant density ρ_l and a temperature-dependent viscosity $\mu(T)$. The surface tension is temperature-dependent but over the range of temperature in the droplet considered in this study, the variation of surface tension is considered negligible [4, 43]. Thereby the Marangoni flow in the droplet is neglected.

The porous substrate is described by porosity, ε , and anisotropic permeability tensor \mathbf{K} . The permeability tensors have the principal axes coinciding with the coordinate axes, r and z . As shown in Figure 1, the liquid droplet profile is denoted by $h(r, t)$ with the contact/spreading radius represented by $R_c(t)$. In the same figure, the infiltration front that separates the wetted region from the dry region in the porous medium is represented by $h_p(r, t)$ with the wetted radius in the porous medium denoted by $R_w(t)$. Across the top surface ($z = 0$) of the porous medium, the droplet and porous medium exchange heat and mass. **Due to the porous medium's open pore structure, gas can move between the pore spaces and the open space above the porous medium. We assume the gas pressure in the dry porous medium the same as the ambient pressure.** As a CMAS droplet crosses the interface, the pressure above the porous medium P_l is equal to the pressure inside the porous medium P_p :

$$P_p = P_l = P \quad \text{at } z = 0 \quad (1)$$

For the sake of simplicity, P is used to represent the pressure in both liquid and porous medium in this study. In an anisotropic porous medium with in-plane homogeneity, the infiltration is described by the combined mass conservation and Darcy's equation, which is:

$$\frac{1}{r} \frac{\partial(r u_p)}{\partial r} + \frac{\partial w_p}{\partial z} = 0 \quad (2)$$

$$u_p = -\frac{K_{rr}}{\mu} \frac{\partial P}{\partial r}, \quad w_p = -\frac{K_{zz}}{\mu} \frac{\partial P}{\partial z} \quad (3)$$

where u_p and w_p are the average velocity in the porous medium in radial and axial directions, respectively, and K_{rr} and K_{zz} are the radial and vertical components of the anisotropic permeability tensor \mathbf{K} , respectively. The combined equation is solved to determine the pressure field:

$$\frac{1}{r} \frac{\partial}{\partial r} \left(r \frac{K_{rr}}{\mu} \frac{\partial P}{\partial r} \right) + \frac{\partial}{\partial z} \left(\frac{K_{zz}}{\mu} \frac{\partial P}{\partial z} \right) = 0 \quad (4)$$

The infiltration front in the porous medium is tracked by a color function c , which is defined as $c = 1$ in the wetted region and $c = 0$ in the dry region, and is solved by a transient advection equation:

$$\frac{\partial(\varepsilon c)}{\partial t} + \frac{1}{r} \frac{\partial}{\partial r} (r u_p c) + \frac{\partial}{\partial z} (w_p c) = 0 \quad (5)$$

The capillary pressure P_c acting at the infiltration front is expressed as:

$$P_c = -\frac{2\sigma \cos \theta_e}{r_c} \quad (6)$$

where σ , r_c , and θ_e are surface tension, the effective capillary radius of the pore, and the equilibrium contact angle between the liquid and the solid material, respectively.

Above the porous medium, the lubrication approximation is used. For the spreading or receding of a thin sessile droplet above an impermeable surface, it is:

$$\frac{\partial h}{\partial t} = \frac{1}{3\mu r} \frac{\partial}{\partial r} \left(r h^3 \frac{\partial P}{\partial r} \right) \quad (7)$$

To describe the simultaneous droplet spreading and infiltration, Eq. (7) is modified to account for the mass flow from the sessile droplet into the porous medium at the top surface $z = 0$, which is:

$$\frac{\partial h}{\partial t} = \frac{1}{3\mu r} \frac{\partial}{\partial r} \left(r h^3 \frac{\partial P}{\partial r} \right) - w_p|_{z=0} \quad (8)$$

In the lubrication model, pressure in the liquid arises from hydrostatic pressure and surface tension. In addition, the disjoining pressure Π_c is incorporated to model the wetting interactions between the liquid and solid at the contact line.

The hydrostatic pressure P_g at any radial location in the droplet is a function of the local height of the droplet and therefore:

$$P_g = \rho_l g h \quad (9)$$

where g is gravitational acceleration. Pressure due to surface tension P_σ is related to the curvature γ of the droplet through the Young-Laplace equation:

$$P_\sigma = -\sigma \gamma \quad (10)$$

Using the thin droplet approximation, the curvature is approximated as:

$$\gamma = \nabla \cdot \vec{n} = \frac{1}{r} \frac{\partial}{\partial r} \left(r \frac{\partial h}{\partial r} \right) \quad (11)$$

where \vec{n} is the unit normal vector of the droplet surface pointing outwards.

At the contact line, the wetting force is modeled by introducing the concept of a thin precursor film h^* that is orders of magnitude thinner than the droplets and an associated disjoining pressure Π_c [44]. Physically, the precursor film concept follows observations that a fast-spreading liquid film of thickness h^* forms on the surface upon droplet contact as shown in Figure 2, which is $h = h^*$ for $r \gg R_c$ [45]. As a function of the liquid thickness h as well as the liquid properties, the disjoining pressure is only non-trivial near the contact line of the droplet. Schwartz and Eley [44] used the following equation to calculate the disjoining pressure:

$$\begin{aligned} \Pi_c &= E \left[\left(\frac{h^*}{h} \right)^{n_\Pi} - \left(\frac{h^*}{h} \right)^{m_\Pi} \right], \quad n_\Pi > m_\Pi > 1 \\ E &\approx \frac{1}{h^*} \frac{(n_\Pi - 1)(m_\Pi - 1)}{2(n_\Pi - m_\Pi)} \sigma \theta_e^2 \end{aligned} \quad (12)$$

The first term for Π_c with exponent n_Π represents the repulsive forces between the liquid and substrate while the second term with exponent m_Π represents the conjoining forces. The constant E represents the strength of interaction through the surface tension and equilibrium contact angle. In most studies, $n_\Pi = 3$ and $m_\Pi = 2$ are used due to the consideration of overall stability and computational cost [25, 31]. The value of h^* can be ascertained from experimental and theoretical data [25, 31]. Unfortunately, experimental data on CMAS wetting interactions are limited. Based on a trial-and-error approach, an h^* value of 200 nm is used as it allows the lubrication model to replicate the equilibrium contact angle used in Eq. (12).

To summarize, the pressure in Eq. (8) can be expressed as:

$$P = \rho_l g h - \frac{\sigma}{r} \frac{\partial}{\partial r} \left(r \frac{\partial h}{\partial r} \right) - \Pi_c \quad (13)$$

The droplet spreading above the surface is solved over a domain of $0 \leq r < L$, where L is much larger than the maximum droplet spreading diameter to avoid constraining the contact line. The boundary conditions for the fourth-order differential equation Eq. (7)(7) are:

$$\left. \frac{\partial h}{\partial r} \right|_{r=0} = 0, \quad \left. \frac{\partial^3 h}{\partial r^3} \right|_{r=0} = 0, \quad h_{r=L} = h^*, \quad \left. \frac{\partial h}{\partial r} \right|_{r=L} = 0 \quad (14)$$

We assume that before infiltration starts, the sessile droplet is in equilibrium with the substrate and that the initial shape of the droplet takes a hemispheric shape as given by:

$$h(r, t = 0) = \begin{cases} h_0 \left(1 - \left(\frac{r}{R_{c,0}} \right)^2 \right) + h^*, & r < R_{c,0} \\ h^*, & r \geq R_{c,0} \end{cases} \quad (15)$$

where $R_{c,0}$ is the initial contact radius and h_0 is the initial center droplet height. $R_{c,0}$ and h_0 are determined by θ_e and the volume of the droplet. For CMAS, a thin droplet requirement is satisfied due to the small value of θ_e , which is 13° for CMAS on 7YSZ. The dynamic contact angle $\theta(t)$ during droplet spreading/receding is defined using the minimum slope of the droplet height profile as given Figure 2:

$$\theta(t) = -\tan^{-1} \left(\min \left(\frac{\partial h}{\partial r} \right) \right) \quad (16)$$

The transient contact radius $R_c(t)$ is calculated by extrapolating the tangent of the minimum slope to the interface $h = 0$, as shown in Figure 2.

Simultaneous with the droplet spreading, Eqs. (4) and (5) are solved for the CMAS infiltration over a cylindrical domain with a dimension $0 \leq r < L$ and $0 \leq z < H$, where H is the thickness of the porous topcoat. Mass conservation across the top porous surface is enforced via the sink term in Eq. (8), $w_p|_{z=0}$. Based on Eq. (1), the boundary condition at the top surface wetted by the droplet is:

$$P = \rho_l g h - \frac{\sigma}{r} \frac{\partial}{\partial r} \left(r \frac{\partial h}{\partial r} \right) - \Pi_c \text{ at } z = 0, \quad 0 \leq r \leq R_c \quad (17)$$

Outside of the contact radius at the top surface of the TBC, there is zero mass flux across the top surface so the boundary condition is:

$$\frac{\partial P}{\partial z} = 0, \quad \text{at } z = 0, \quad R_c < r < L. \quad (18)$$

At the infiltration front, $P = P_c$. At the remaining boundaries, $P = 0$. An initially dry porous medium is assumed except for the top surface in contact with the droplet:

$$c(r, z, t = 0) = 0, \quad c(r \leq R_c, z = 0, t) = 1 \quad (19)$$

At the remaining three boundaries $c = 0$.

3. Heat Transfer for Droplet Spreading and Infiltration

The temperature across the thickness of the TBC topcoat varies significantly due to the low temperature of the underlying turbine blade and the high temperature of the turbine gases. As the viscosity of the CMAS melt is highly temperature-dependent, such a steep temperature gradient may have a substantial influence on the fluid flow in the spreading droplet and porous medium. On the other hand, the progression of the CMAS infiltration changes the thermal properties of the porous topcoat as the wetted region has a higher thermal conductivity and capacity than the dry medium. Therefore, it is critical to incorporate simultaneous heat transfer in the investigation of CMAS infiltration.

As shown in Figure 3, the bottom surface temperature T_b is assumed to be a constant value determined by the internal cooling. A heat flux q_s'' is applied to the top surface of the topcoat to mimic the combined convective and radiative heating from the high temperature environment due to the unavailable information on the heating conditions. A steady-state temperature distribution across the dry topcoat before droplet impact is used as the initial temperature distribution. For a homogeneous material, it has the form of:

$$T(r, z, t = 0) = \frac{q_s''}{k_{eff}}(H - z) + T_b \quad (20)$$

where k_{eff} is the effective thermal conductivity. The value of q_s'' is chosen to create the designated initial top surface temperature commonly used in existing studies [14, 15, 41]. We also

approximate that q_s'' is not affected by the presence of the droplet on the topcoat throughout the infiltration process due to the droplet's small size. Solidification behavior for the CMAS formulation used in this study [2] shows that the onset of CMAS solidification during cooling is 1200°C, which is below the lowest CMAS temperature in this study. Therefore, CMAS solidification is not considered in the model.

Numerical simulation of the heat transfer between the droplet and the TBC topcoat could be computationally costly because tracking the diminishing thickness and radius of the droplet requires a very fine mesh. To reduce the computational time without sacrificing the accuracy of the results, a transient one-dimensional heat transfer model is developed considering that the temperature variation across the thickness of the liquid layer is much smaller than that in the radial direction and across the topcoat. This assumption is valid for two reasons: first, due to the small equilibrium contact angle of 13° between CMAS and 7YSZ topcoat [23], the ratio of the droplet height to its contact radius remains low throughout the infiltration process. Moreover, the spreading liquid layer is thinner than the topcoat beneath it by several orders of magnitude. As such, it is acceptable to approximate the temperature in the thin liquid droplet as a function of the radial location and time only, which is $T_l(r, t)$. This approximation enables reduction of the two-dimension problem to a one-dimensional one, analogous to the treatment of momentum in the lubrication model and heat transfer in thin fins. Through derivation based on the principle of energy conservation (further discussed in the Appendix A), we obtain the equation:

$$\begin{aligned} \frac{\partial(\rho_l c_{p,l} h T_l)}{\partial t} + \frac{1}{r} \frac{\partial}{\partial r} (\rho_l c_{p,l} u_l r h T_l) \\ = \frac{1}{r} \frac{\partial}{\partial r} \left(r h k_l \frac{\partial T_l}{\partial r} \right) + q_s'' + k_{eff} \frac{\partial T_p}{\partial z} \Big|_{z=0} - \rho_l c_{p,l} T_l w_p \Big|_{z=0} \end{aligned} \quad (21)$$

$at \ 0 \leq r \leq R_c$

where the subscript l designates liquid and c_p is specific heat. q_s'' represents the energy exchange with the surroundings, and the third and fourth terms represent heat transfer with the topcoat due to conduction and infiltration, respectively. u_l is the liquid velocity in the radial direction due to droplet spreading/receding. This radial flow velocity is found by solving the following mass conservation equation for the droplet:

$$\frac{\partial h}{\partial t} + \frac{1}{r} \frac{\partial}{\partial r} (r h u_l) = -w_p \Big|_{z=0} \quad (22)$$

with the boundary condition applied to the center axis being:

$$u_l = 0 \text{ at } r = 0 \quad (23)$$

Heat transfer in the porous topcoat is a two-dimensional heat transfer problem in the axisymmetric domain, which is described as:

$$\frac{\partial}{\partial t} [(\rho c_p)_{eff} T_p] = \frac{1}{r} \frac{\partial}{\partial r} \left(r k_{eff} \frac{\partial T_p}{\partial r} \right) + \frac{\partial}{\partial z} \left(k_{eff} \frac{\partial T_p}{\partial z} \right) \quad (24)$$

Heat transfer by convection of the molten CMAS is neglected due to the low Péclet number as analyzed in Munuhe et al. [41]. In addition, perfect contact between the spreading droplet and the porous medium is assumed such that:

$$T_l = T_p \text{ at } z = 0 \text{ and } r \leq R_c \quad (25)$$

Substituting Eq. (25) into Eq. (21) for heat transfer in the liquid droplet we arrive at:

$$\begin{aligned} \frac{\partial(\rho_l c_{p,l} h T_p)}{\partial t} + \frac{1}{r} \frac{\partial}{\partial r} (\rho_l c_{p,l} u_l r h T_p) \\ = \frac{1}{r} \frac{\partial}{\partial r} \left(k_l r h \frac{\partial T_p}{\partial r} \right) + q_s'' + k_{eff} \frac{\partial T_p}{\partial z} \Big|_{z=0} - \rho_l c_{p,l} T_p w_p \Big|_{z=0} \end{aligned} \quad (26)$$

$$\text{at } z = 0, r \leq R_c$$

As such, the heat transfer model is reduced to solving for T_p only. Beyond the contact radius, q_s'' is applied to the dry porous medium surface to consider the heat exchange of the top surface with the surroundings, as discussed in the initial thermal conditions of the topcoat:

$$-k_{eff} \frac{\partial T_p}{\partial z} = q_s'' \text{ at } z = 0, r > R_c \quad (27)$$

At the bottom surface of the topcoat $z = H$, $T_p = T_b$. A symmetry boundary condition is applied to the centerline, $r = 0$, in the porous medium, and the boundary condition of the porous medium at $r = L$ is adiabatic:

$$\begin{aligned}\frac{\partial T_p}{\partial r} &= 0 \text{ at } r = 0 \\ \frac{\partial T_p}{\partial r} &= 0 \text{ at } r = L\end{aligned}\tag{28}$$

At the infiltration front in the porous medium, which separates two domains with different thermal properties, continuous temperature and heat flux is enforced. Within the wetted region, the effective thermal conductivity is assumed isotropic, and this assumption is justified by the minimal difference in thermal conductivity between CMAS and 7YSZ [41]. In the dry region, the effective thermal conductivity is supposedly anisotropic due to the columnar microstructure. However, information on the anisotropic thermal conductivity of the 7YSZ porous layer is not available. Considering the low porosity and strong radiation heat transfer across the gaps between columns, heat conduction in the dry region is assumed as isotropic as well. Effective thermal conductivity and specific heat capacity in the wetted region are calculated using the following equations [41]:

$$k_{eff} = \begin{cases} k_{solid} \left(1 + \varepsilon \left(\frac{k_{CMAS}}{k_{solid}} - 1 \right) \right), & \text{infiltrated by CMAS} \\ k_{eff,dry}, & \text{occupied by gas phase} \end{cases}\tag{29}$$

and

$$(\rho c_p)_{eff} = \begin{cases} \varepsilon(\rho c_p)_{CMAS} + (1 - \varepsilon)(\rho c_p)_{solid}, & \text{infiltrated by CMAS} \\ \varepsilon(\rho c_p)_{gas} + (1 - \varepsilon)(\rho c_p)_{solid}, & \text{occupied by gas phase} \end{cases}\tag{30}$$

where *solid* denotes the 7YSZ. The $k_{eff,dry}$ is the experimentally measured thermal conductivity of 7YSZ porous material [52]. Detailed discussion on the choice of effective thermal conductivity correlation can be found in Munu et al. [41].

4. Numerical Issues and Simulation Parameters

4.1 Numerical Issues

The finite volume method is used to solve the mathematical model developed in this study. Due to the highly coupled nature of the physical process, droplet spreading above the surface,

infiltration in the porous medium, and heat transfer in both the droplet and the porous medium are solved for iteratively and implicitly. The modified lubrication equation (Eq. (8)) and heat transfer model (Eq. (26)) are solved first for the droplet profile and temperature distribution, followed by infiltration (Eqs. (4) and (5)) and heat transfer (Eq. (24)) in the porous medium to determine the location and shape of the infiltration front and the CMAS properties. This iterative process continues until convergence is reached. All equations are solved using an in-house developed code in MATLAB. The second-order central-difference scheme is used to discretize the differentiation in space in the fourth-order lubrication equation, the combined continuity and Darcy's equation, and heat transfer equation. Integration in time uses a first-order fully implicit scheme. A first-order upstream scheme is used for the convective term in the color function c for tracking the wetted domain. Through trial and error, a cutoff value of $c = 0.95$ is used to mark the infiltration front based on preservation of the mass conservation and the accuracy of the infiltration rate. A fine time step of $10 \mu\text{s}$ and a mesh size of $2 \mu\text{m}$ is used in this study. Both mesh and time step independence are confirmed by decreasing mesh and time step by a factor of 2 and comparing infiltration profiles at different times. Results indicate differences less than 1% in the infiltration and droplet profiles at any given time.

Validation consists of two test cases: the first is viscous droplet spreading on impermeable substrates to confirm that wetting interactions are modeled accurately and that spreading dynamics follow Tanner's law, as suggested by experimental findings by [22]. The second test problem is uniform film infiltration to confirm that the combined lubrication theory-color function tracking approach produces accurate infiltration dynamics and conservation of mass. Results and discussion for these cases are presented in Appendix B.

4.2 Properties and Simulation Parameters

Droplet size and initial temperature are set based on likely scenarios in gas turbines [12]. CMAS droplets impacting TBCs in aero-gas turbines are constrained in size by the turbine's filtration system that removes particles greater than $70 \mu\text{m}$ in diameter and smaller droplets (less than $15 \mu\text{m}$) are likely to become entrained in flow [12]. Additionally, this study only considers fully melted droplets, which further limits the size of droplets between $15 \mu\text{m}$ and $60 \mu\text{m}$ [12]. In this study, a CMAS droplet diameter of $54 \mu\text{m}$ is used. CMAS particles are heated and melted as they are carried by hot gas in the turbine at temperatures in excess of 1400°C in aero-gas turbines.

Because of the phase change and the short time particles stay in the hot turbine gas prior to impact, the particle temperature upon impact could be less than the freestream temperature [12]. In this investigation, the initial temperature of the CMAS droplet varies around 1300°C, representing fully melted droplets.

The problem setup and thermal boundary and initial conditions are presented schematically in Figure 1 and Figure 3, respectively. Initial droplet and topcoat conditions, geometries and properties used in the simulation are given in Table 1 and Table 2. A bottom temperature of 1100°C is chosen and a value of 700 kW/m² is selected for q_s'' to achieve an initial top surface temperature of 1250°C based on the studies of CMAS infiltration in a TBC topcoat [15, 41].

As an EB-PVD 7YSZ topcoat has parallel columns with roughly quadrilateral cross-sections perpendicular to the substrate [16], it is anisotropic with different permeability in the radial and vertical directions. Knowledge of the permeability of the EB-PVD 7YSZ topcoat is limited so Naraparaju et al. [16] approximated the columns as solid cylinders with annular gaps around them and employed a correlation developed by Dvorkin [46] for the permeability in the vertical direction of such a structure:

$$K = \frac{\varepsilon D_o^2}{32\tau^2} \left[1 + \left(\frac{D_i}{D_o} \right)^2 + \left(1 - \left(\frac{D_i}{D_o} \right)^2 \right) \frac{1}{\ln \left(\frac{D_i}{D_o} \right)} \right] \quad (31)$$

where D_o is the outer diameter of the annular gap and D_i is the column diameter. τ is tortuosity that stems from the microstructure variances due to the random orientation, size, and shape of the columns. Despite the bold simplifications for the porous structure, Naraparaju et al. [16] predicted infiltration rates consistent with the experimental observations for isothermal tests [17]. Therefore, Eq. (31) is used in this study to determine the permeability in the vertical direction. More information about the approximation of D_o , D_i , and τ can be found in previous publications [16, 41].

In the radial direction, the permeability is heavily influenced by the placement of the columns and their orientation [47] and may vary over a large range. In the absence of measured permeability, the material anisotropy is represented by a ratio of $K_{rr}/K_{zz} = F$, with F as a constant factor [25]. In this study, we consider three different cases to investigate the effect of anisotropic properties of the column structures on CMAS infiltration: base anisotropy with $K_{rr} = K_{zz}/10$, isotropic infiltration with $K_{rr} = K_{zz}$, and infiltration in the vertical direction only with $K_{rr} = 0$.

For liquid infiltration in a very narrow annular gap, the effective capillary radius used in Eq. (6), r_c , can be approximated as half of the gap width:

$$r_c = \frac{D_o - D_i}{2} \quad (32)$$

Also, one CMAS composition, desert sand derivative, is used. The viscosity-temperature relationship is considered through the Giordano model [48]:

$$\log \mu = A + \frac{B}{T - C} \quad (33)$$

where A , B , and C are variables dependent on CMAS composition and T is the CMAS temperature in units Kelvin. These constants and other thermal and material properties used in this study are given in Table 2 and Table 3.

5. Results

5.1 Baseline Case

A droplet spreading and infiltrating into a porous TBC topcoat is simulated in the porous medium with an anisotropy ratio $K_{rr} = K_{zz}/10$. At $t = 0$, the droplet temperature T_d is 1300°C, higher than the top surface temperature of 1250°C. Temperatures along the vertical centerline $r = 0$ at different times are compared in Figure 4. At $t = 50 \mu\text{s}$, the top surface is elevated to 1290°C, but the thermal penetration depth is limited to 20 μm . At $t = 1 \text{ s}$, the top surface temperature drops to its initial temperature of about 1250°C. While the droplet is not fully absorbed until $t = 18.4 \text{ s}$, the heating by the droplet lasts less than one second. In Figure 4, discontinuous temperature gradients can be observed at $t = 1, 10$ and 18.4 s . These discontinuities in the vertical thermal profiles indicate the location of the infiltration front, as the two regions have different thermal conductivities. Within each region, wetted or dry, the vertical temperature distribution is quasi-linear. The infiltrated region has a smaller temperature gradient due to a higher thermal conductivity associated with CMAS infiltration. For the same reason, the presence of the wetted region enhances the overall thermal conductivity of the topcoat, leading to a slightly decreased temperature in the droplet over time. As the infiltration continues, the temperature at the infiltration front decreases due to a stronger cooling from the cold bottom surface, thus leading to a higher local CMAS viscosity.

Transient droplet spreading and infiltration dynamics as represented by the liquid droplet height, infiltration depth, and droplet contact and wetted radius are shown in Figure Figure 5. For the anisotropic topcoat ($K_{rr} = K_{zz}/10$), the decrease of the droplet height $h(t)$ shown in Figure 5(a) can be characterized by three stages: initial fast decrease, slow quasi-linear intermediate decrease, and late-stage fast decrease. The contact radius $R_c(t)$ of the droplet as shown in Figure 5(c) recedes in a similar manner to the droplet height, with both results reflecting the molten mass being absorbed by the porous topcoat. These rapid decreases in $h(0,t)$ and $R_c(t)$ during the early stage corroborate the rapid increase in infiltration depth ($h_p(0,t)$) shown in Figure 5(b). The fast penetration at the beginning of the infiltration process can be explained by the high pressure gradient in the vertical direction when the infiltration depth is thin, on the order of $P_c/h_p(0,t)$. However, as the infiltration front advances, the vertical pressure gradient diminishes quickly. Meanwhile, there is an increase in the CMAS viscosity near the infiltration front corresponding to the decreasing infiltration front temperature, as presented in Figure 4. As a result, the vertical infiltration slows down. While it takes 0.5 s to reach 10 μm , it takes 2 s to reach 20 μm , a 73% percent decrease in average infiltration velocity. The reduced infiltration rate leads to a slow decrease in the droplet height and contact radius recession, as already observed and discussed for Figures 5(a) and (c).

Towards the end of infiltration, the pressure in the droplet due to surface tension increases as the droplet shrinks in size, rapidly driving the liquid into the porous medium. This process also corroborates the rapid recession in $R_c(t)$, as shown in Figure 5(c). However, this fast absorption causes no substantial change in the infiltration rate due to the diminishing volume of the droplet. The wetted radius $R_w(t)$ is shown in Figure 5(d). For droplet infiltration into the anisotropic topcoat with $K_{rr} = K_{zz}/10$, $R_w(t)$ remains nearly constant, illustrating the limited lateral infiltration due to the large anisotropy ratio of the permeability.

The base anisotropic case is compared against an isotropic porous medium ($K_{rr} = K_{zz}$) and a medium which only allows vertical infiltration ($K_{rr} = 0$), shown in Figure 5. Although the droplet height $h(0,t)$ and contact radius $R_c(t)$ exhibit three stages similar to those observed in the baseline case ($K_{rr} = K_{zz}/10$), increased anisotropy corresponds with slower contact line recession and droplet height decrease. Moreover, the wetted radius shown in Figure 5(d) only becomes wider when the porous medium is isotropic, and the results with a $K_{rr} = K_{zz}/10$ ratio are close to a purely

vertical infiltration case. The infiltration rates shown in Figure 5(b) for three cases are consistent, despite the deeper final penetration depths for the more anisotropic topcoats.

The evolution of the droplet and infiltration profile for the base anisotropy ratio of $K_{rr} = K_{zz}/10$ is shown in Figures 6(a-e). With the contact line recession, the droplet maintains a relatively consistent contact angle. In the porous medium, the wetted region starts with a wide and mostly flat base at $t = 1$ s, but becomes more rounded as the flat bottom narrows corresponding with the receding droplet contact area. Such a strong influence of the contact line behavior on the infiltration width is attributed to the limited radial infiltration in the anisotropic porous medium ($K_{rr} = K_{zz}/10$). The pressure distributions in the wetted medium at $t = 10$ s and 18 s, presented in Figure 7(a) and (b), respectively, reveal a steep radial pressure gradient in a narrow annulus outside the contact radius due to the low radial permeability of the medium. In the vertical direction, a large pressure gradient can be observed underneath the shrinking droplet. With the recession of the droplet contact radius, the vertical infiltration becomes increasingly localized within the diminishing contact area, leading to a reducing width of the wetted profile along z towards the end of the process as shown in Figures 6 (b – e).

A comparison of the final infiltration profiles in the topcoat of various degrees of anisotropy is shown in Figure 6(e). The radial infiltration in the isotropic medium $K_{rr} = K_{zz}$ gives rise to a wider wetted area with time, thus limiting the vertical penetration. The deeper and slightly narrower final infiltration profile of the medium with $K_{rr} = 0$ compared to the medium with $K_{rr} = K_{zz}/10$ reveals that, despite the constant wetting radii of the two cases, radial infiltration is occurring slowly.

5.2 Effects of Initial Droplet Temperature and Temperature Gradient in the Topcoat

Heat transfer is critical to CMAS droplet infiltration because CMAS viscosity is highly temperature-dependent, as described in Eq. (33). Both the droplet initial temperature and top surface temperature of the TBCs change depending on the hot gas temperature in a turbine. It is of interest to evaluate how the droplet initial temperature and temperature variation in the topcoat affects the infiltration dynamics and final infiltration profile.

In this study, we investigate the effect of these thermal conditions through four different cases described in Table 4. The first three cases are used to test droplets initially at 1250°C, 1300°C and

1400°C, respectively. The viscosities of CMAS droplets μ_d at those temperatures are also given in Table 4. Apart from the initial droplet temperature, these cases share the same initial and boundary conditions of the topcoats and TBC properties described in Tables 1, 2 and 4. In Case 4, the droplet and the entire topcoat have the same temperature of 1250°C, mimicking the isothermal experimental conditions commonly used in literature [16, 17, 50]. In all cases, the anisotropic permeability ratio is $K_{rr} = K_{zz}/10$.

Transient infiltration depth and final infiltration profiles for cases 1 – 3 presented in Figure 8 show that the initial droplet temperature has a negligible effect on the infiltration rate and the final infiltration shape. This is consistent with the rapid dissipation of the droplet's thermal energy and its insignificant influence on the long-term heat transfer process as shown in Figure 4. Droplet infiltration in the isothermal topcoat (Case 4) has the same dynamics in the initial stage but allows faster infiltration over the long term. The divergence is most noticeable after two seconds, highlighting the influence of the bottom temperature on infiltration at the later stage of the droplet sorption. The final infiltration profiles of all four cases in Figure 8(b) overlap so the topcoat thermal conditions only seem to affect infiltration rates.

5.3 Effect of Porous Medium Microstructure

Depending on the design and deposition process, the microstructure of an EB-PVD 7YSZ topcoat can vary significantly [50]. The effect of pore size and heterogeneous structures on the infiltration of a large reservoir of CMAS was investigated using a one-dimensional multilayer model [41]. However, quantitative information and understanding of CMAS droplet spreading and infiltration in heterogeneous columnar structure remains limited. Specifically, the two-dimensional droplet will have an infiltration front divided between the two layers, which will affect the infiltration process to an unknown degree.

In this study, the droplet infiltration is simulated in three topcoats: a single layer with fine columns, a single layer with coarse columns, and a bilayer consisting of a fine-column layer that is 30 μm thick deposited on top of a coarse-column bottom layer, as shown in Figure 9(a). As given in Table 5, a coarse columnar structure refers to a column diameter $D_i = 12.7 \mu\text{m}$ and a gap size of 1.7 μm , whereas a fine columnar structure has a column diameter $D_i = 6.4 \mu\text{m}$ and a gap size of 0.8 μm . Both fine and coarse structures have the same total topcoat thickness $H = 300 \mu\text{m}$,

porosity $\varepsilon = 0.15$, and anisotropy ratio $K_{rr} = K_{zz}/10$. Thermophysical properties used in this study are solely porosity-dependent, and thus remain unchanged as given in Table 2. Initial and boundary conditions as given in Table 1 are used in the simulation. With constant porosity, the smaller column diameter and spacing decreases permeability in both the radial and vertical directions but increases capillary pressure substantially, as given in Table 5.

Infiltration dynamics and final infiltration profiles in the three topcoats are presented in Figure 10 and the pressure fields in the three topcoats after the infiltration front has reached the bottom layer at $36 \mu\text{m}$ depth are compared in Figure 11. The vertical pressure gradient is a factor-of-two higher than the coarse structure as compared in Figure 11(a) and (b), respectively. Meanwhile, the fine structure offers more resistance to infiltration. The slower infiltration rate in the fine single layer compared to the coarse single layer, as shown in Figure 10(b), demonstrates the dominant role of the increased permeability over the capillary pressure when porosity remains constant.

The rates of droplet height decrease, contact radius recession, and infiltration in the bilayer structure, represented by the blue curves in Figures 10(a-c), respectively, are slower than the coarse single layer, but overlap those in the fine single layer before $z = 30 \mu\text{m}$ due to identical structure. However, beyond the fine top layer, the infiltration abruptly slows down (Figure 10(b)), in correspondence with reduced rates of the droplet height decrease and the recession of the contact radius (Figure 10(a,c)). The sharp transition in both observable droplet parameters suggests that they can be used to estimate when the infiltration front has reached the bilayer's interior interface.

The infiltration rate abruptly slows down in the bottom part of the bilayer due to a unique combination of a low capillary pressure and a high total resistance to infiltration. Once the infiltration front crosses the interior interface between the fine and coarse structures at $z = 30 \mu\text{m}$, the capillary pressure drops such that the bilayer structure has approximately the same vertical pressure gradient as the coarse single layer, as shown in Figures 11(a) and (c). On the other hand, the $30 \mu\text{m}$ -thick fine structure still offers extra resistance to infiltration along the path. As a result, the bilayer structure leads to a prolonged total infiltration time of 48.4 s , in comparison to 18.4 s and 35.1 s in the coarse and fine single layers, respectively.

Also of interest is whether and how the final droplet infiltration profile is affected by the bilayer structure. Figure 10(d) shows that the bilayer structure leads to a slightly wider wetted medium above $z = 30 \mu\text{m}$ than both single layers. This is mainly due to the prolonged total infiltration time in the bilayer that allows more time for lateral infiltration in the region above $z = 30 \mu\text{m}$. Figures

11(b) and (c) show that the lateral pressure gradients in the bilayer and the single fine layer are approximately the same above $z = 30 \mu\text{m}$ because of identical microstructural features. Thereby, the lateral infiltration rates of both structures in this region should be close to each other. It is also observed that extra lateral infiltration in the bilayer leads to a decreased wetted volume below the top layer compared to the single-layer topcoats. Thus, reduced infiltration depth is anticipated with a reduced anisotropy ratio $K_{rr} > K_{zz}/10$. The final infiltration profiles in the homogeneous single layers remain invariant despite the different capillary pressures at the infiltration front and the transport properties of the media.

5.4 Multilayer Structure

In addition to the bilayer structure, simulations are also conducted to study spreading and infiltration of a single droplet in a multilayer topcoat where three $10 \mu\text{m}$ -thick fine structured layers are embedded $10 \mu\text{m}$ apart in the coarse structure, as shown in Figure 9(b). The structural and transport properties of the fine and coarse structure are given in Table 5. Apart from the multilayer structure, other parameters used in the simulation such as the total topcoat thickness, porosity, anisotropy, and initial and boundary conditions remain the same as the bilayer. Besides, the multilayer coat has the same total thickness of the fine structure ($H_0 = 30 \mu\text{m}$).

Figure 12 compares the infiltration dynamics and final wetting profiles of the bilayer and multilayer topcoats. Vertical infiltration begins to slow down earlier in the multilayer topcoat between infiltration depths $10 \mu\text{m} < h_p(0,t) < 30 \mu\text{m}$, as shown in Figure 12(b). The multilayer's advantage in delaying infiltration diminishes when both cases reach an infiltration depth of $30 \mu\text{m}$. Below the bilayer's top layer thickness ($z = 30 \mu\text{m}$), the bilayer structure hinders the infiltration better than the multilayer structure.

The multilayer's droplet height $h(0,t)$ (Figure 12(a)) and contact radius $R_c(t)$ (Figure 12(c)) show a sharp change when the infiltration front reaches the first interior interface. Apart from the initial transition at $10 \mu\text{m}$, the remaining transitions are much more subtly conveyed by the droplet height and radius, with the 40 and $50 \mu\text{m}$ transitions being almost imperceptible. It can be seen in Figure 12(d) that the final infiltration profiles and depth for both the bilayer and the multilayer structure appear to be approximately the same. This result is similar to those shown in Figures 8(b) and 10(d), suggesting that different structures result in different infiltration rates while the overall droplet mass/volumen conservation is observed, further validating the simulation. Observations in

this study are consistent with a previous study with a one-dimensional infiltration model [41], which shows that multilayer structures have superior infiltration prevention to monolayer and bilayer over short distances from the top surface.

5.5 Limitations

One limitation of this study is the constant heat flux boundary condition assumed on the surface of the topcoat to create the top surface temperature commonly used in the experimental study. In reality, the impact of the droplet may alter the convection and radiation heat transfer with the surrounding. This can be improved in the future study if relevant information becomes available. Another limitation of this study is the simplified column structures for evaluation of the hydraulic permeability and capillary pressure due to the limited knowledge of the transport properties of 7YSZ topcoats grown by the EB-PVD method. The anisotropic structure is represented by the ratio of $K_{rr} = FK_{zz}$ with F as a constant. Sophisticated structures such as smaller columns protruding from the main columns at an angle are considered by an estimated constant tortuosity. Additionally, the assumption of constant porosity for the heterogeneous structures is a simplification. Further, the current axisymmetric model does not address the centrifugal force due to the high-speed rotation of the turbine blade. To address the limitations due to geometry or porous medium characterization, this study will be continued by extending the two-dimensional model to three-dimensions and progressively including more realistic boundary conditions and anisotropic material properties.

Validation with experimental study will be valuable to support the simulation results. However, to the authors' best knowledge, experimental studies of micron-sized CMAS droplet sorption in a non-isothermal layer of 7YSZ have not been reported by other groups. Our previous study [41] of a one-dimensional infiltration using the same set of relationship predicts infiltration rates consistent with experimental observations.

6. Conclusion

An integrated model considering droplet spreading, wetting, transient heat transfer, and infiltration of a liquid with temperature-dependent viscosity is used to investigate CMAS droplet spreading and infiltration into anisotropic and heterogeneous porous structures. The current CMAS

infiltration model can be used to optimize microstructure parameters to limit infiltration. The model can also be extended to consider phase change and chemical reactions with the topcoat material. Additionally, the model's flexibility with regards to material properties allows investigation of CMAS interactions with novel TBC materials, which are a frequent focus of experimental CMAS infiltration studies. The main points are summarized as follows:

- (1) This study shows that CMAS droplets of a size encountered by real gas turbines will lose their initial thermal energy soon after impact on a TBC and have negligible influence on the overall infiltration behavior.
- (2) The temperature gradient within the TBC topcoat has a substantial impact on the CMAS infiltration rate. An anisotropic microstructure can significantly affect the lateral spreading and final penetration depth but has an insignificant influence on the initial infiltration rate.
- (3) Heterogeneous structures such as bilayer and multilayer structures can limit and delay vertical infiltration by diminishing the vertical pressure gradient and increasing the resistance to fluid flow. While a bilayer structure has slower overall infiltration, a multilayer structure will experience infiltration deceleration earlier.

Acknowledgements

The hardware used in the computational studies is part of the UMBC High Performance Computing Facility (HPCF). This research was supported in part by the National Science Foundation research grant CBET-1705538.

References

- [1] Krämer, S., Faulhaber, S., Chambers, M., Clarke, D., Levi, C., Hutchinson, J., and Evans, A., 2008, "Mechanisms of cracking and delamination within thick thermal barrier systems in aero-engines subject to calcium-magnesium-alumino-silicate (CMAS) penetration," *Materials Science and Engineering: A*, 490(1-2), pp. 26-35. <https://doi.org/10.1016/j.msea.2008.01.006>
- [2] Borom, M. P., Johnson, C. A., and Peluso, L. A., 1996, "Role of environment deposits and operating surface temperature in spallation of air plasma sprayed thermal barrier coatings," *Surface and Coatings Technology*, 86, pp. 116-126. [https://doi.org/10.1016/S0257-8972\(96\)02994-5](https://doi.org/10.1016/S0257-8972(96)02994-5)

- [3] Mohan, P., Yuan, B., Patterson, T., Desai, V. H., and Sohn, Y. H., 2007, "Degradation of yttria-stabilized zirconia thermal barrier coatings by vanadium pentoxide, phosphorous pentoxide, and sodium sulfate," *Journal of the American Ceramic Society*, 90(11), pp. 3601-3607. <https://doi.org/10.1111/j.1551-2916.2007.01941.x>
- [4] Krämer, S., Yang, J., Levi, C. G., and Johnson, C. A., 2006, "Thermochemical interaction of thermal barrier coatings with molten CaO–MgO–Al₂O₃–SiO₂ (CMAS) deposits," *Journal of the American Ceramic Society*, 89(10), pp. 3167-3175. <https://doi.org/10.1111/j.1551-2916.2006.01209.x>
- [5] Bansal, N. P., and Choi, S. R., 2015, "Properties of CMAS glass from desert sand," *Ceramics International*, 41(3), pp. 3901-3909. <https://doi.org/10.1016/j.ceramint.2014.11.072>
- [6] Yin, B., Liu, Z., Yang, L., Wu, R., and Zhou, Y., 2019, "Factors influencing the penetration depth of molten volcanic ash in thermal barrier coatings: Theoretical calculation and experimental testing," *Results in Physics*, p. 102169. <https://doi.org/10.1016/j.rinp.2019.102169>
- [7] Qu, W., Li, S., Chen, Z., Li, C., Pei, Y., and Gong, S., 2020, "Hot corrosion behavior and wettability of calcium–magnesium–alumina–silicate (CMAS) on LaTi₂Al₉O₁₉ ceramic," *Corrosion Science*, 162, p. 108199. <https://doi.org/10.1016/j.corsci.2019.108199>
- [8] Wellman, R., Whitman, G., and Nicholls, J. R., 2010, "CMAS corrosion of EB PVD TBCs: Identifying the minimum level to initiate damage," *International Journal of Refractory Metals and Hard Materials*, 28(1), pp. 124-132. <https://doi.org/10.1016/j.ijrmhm.2009.07.005>
- [9] Zhang, X. F., Zhou, K. S., Liu, M., Deng, C. M., Deng, C. G., and Deng, Z. Q., 2016, "Adsorbability and spreadability of calcium-magnesium-alumino-silicate (CMAS) on Al-modified 7YSZ thermal barrier coating," *Ceramics International*, 42(16), pp. 19349-19356. <https://doi.org/10.1016/j.ceramint.2016.09.106>
- [10] Yarin, A. L., 2006, "Drop impact dynamics: splashing, spreading, receding, bouncing...", *Annu. Rev. Fluid Mech.*, 38, pp. 159-192. <https://doi.org/10.1146/annurev.fluid.38.050304.092144>
- [11] Jain, N., Bravo, L., Bose, S., Kim, D., Murugan, M., Ghoshal, A., and Flatau, A., "Turbulent multiphase flow and particle deposition of sand ingestion for high-temperature turbine blades," *Proc. Proceedings of the Summer Program*, p. 1.
- [12] Song, W., Yang, S., Fukumoto, M., Lavallée, Y., Lokachari, S., Guo, H., You, Y., and Dingwell, D. B., 2019, "Impact interaction of in-flight high-energy molten volcanic ash droplets

- with jet engines," *Acta Materialia*, 171, pp. 119-131. <https://doi.org/10.1016/j.actamat.2019.04.011>
- [13] Zhu, Z., 2019, "Study of Volcanic Ash Impact onto Turbine Blades in Jet Engines," Ph.D., University of Surrey (United Kingdom).
- [14] Jackson, R. W., Zaleski, E. M., Hazel, B. T., Begley, M. R., and Levi, C. G., 2017, "Response of molten silicate infiltrated Gd₂Zr₂O₇ thermal barrier coatings to temperature gradients," *Acta Materialia*, 132, pp. 538-549. <https://doi.org/10.1016/j.actamat.2017.03.081>
- [15] Jackson, R. W., Zaleski, E. M., Poerschke, D. L., Hazel, B. T., Begley, M. R., and Levi, C. G., 2015, "Interaction of molten silicates with thermal barrier coatings under temperature gradients," *Acta Materialia*, 89, pp. 396-407. <https://doi.org/10.1016/j.actamat.2015.01.038>
- [16] Naraparaju, R., Hüttermann, M., Schulz, U., and Mechnich, P., 2017, "Tailoring the EB-PVD columnar microstructure to mitigate the infiltration of CMAS in 7YSZ thermal barrier coatings," *Journal of the European Ceramic Society*, 37(1), pp. 261-270. <https://doi.org/10.1016/j.jeurceramsoc.2016.07.027>
- [17] Naraparaju, R., Gomez Chavez, J. J., Niemeyer, P., Hess, K.-U., Song, W., Dingwell, D. B., Lokachari, S., Ramana, C. V., and Schulz, U., 2019, "Estimation of CMAS infiltration depth in EB-PVD TBCs: A new constraint model supported with experimental approach," *Journal of the European Ceramic Society*, 39(9), pp. 2936-2945. <https://doi.org/10.1016/j.jeurceramsoc.2019.02.040>
- [18] Kang, Y. X., Bai, Y., Du, G. Q., Yu, F. L., Bao, C. G., Wang, Y. T., and Ding, F., 2018, "High temperature wettability between CMAS and YSZ coating with tailored surface microstructures," *Materials Letters*, 229, pp. 40-43. <https://doi.org/10.1016/j.matlet.2018.06.066>
- [19] Li, B., Chen, Z., Zheng, H., Li, G., Li, H., and Peng, P., 2019, "Wetting mechanism of CMAS melt on YSZ surface at high temperature: First-principles calculation," *Applied Surface Science*, 483, pp. 811-818. <https://doi.org/10.1016/j.apsusc.2019.04.009>
- [20] Yang, S., Song, W., Lavalée, Y., Zhou, X., Dingwell, D. B., and Guo, H., 2020, "Dynamic spreading of re-melted volcanic ash bead on thermal barrier coatings," *Corrosion Science*, 170, p. 108659. <https://doi.org/10.1016/j.corsci.2020.108659>
- [21] Song, W., Hess, K. U., Damby, D. E., Wadsworth, F. B., Lavallée, Y., Cimorelli, C., and Dingwell, D. B., 2014, "Fusion characteristics of volcanic ash relevant to aviation hazards," *Geophysical Research Letters*, 41(7), pp. 2326-2333. <https://doi.org/10.1002/2013GL059182>

- [22] Song, W., Lavallee, Y., Wadsworth, F. B., Hess, K.-U., and Dingwell, D. B., 2017, "Wetting and spreading of molten volcanic ash in jet engines," *The journal of physical chemistry letters*, 8(8), pp. 1878-1884. <https://doi.org/10.1021/acs.jpcclett.7b00417>
- [23] Zhang, B., Song, W., and Guo, H., 2018, "Wetting, infiltration and interaction behavior of CMAS towards columnar YSZ coatings deposited by plasma spray physical vapor," *Journal of the European Ceramic Society*, 38(10), pp. 3564-3572. <https://doi.org/10.1016/j.jeurceramsoc.2018.04.013>
- [24] Lokachari, S., Song, W., Yuan, J., Kaliwoda, M., and Dingwell, D. B., 2020, "Influence of molten volcanic ash infiltration on the friability of APS thermal barrier coatings," *Ceramics International*, 46(8, Part A), pp. 11364-11371. <https://doi.org/10.1016/j.ceramint.2020.01.166>
- [25] Alleborn, N., and Raszillier, H., 2004, "Spreading and sorption of a droplet on a porous substrate," *Chemical Engineering Science*, 59(10), pp. 2071-2088. <https://doi.org/10.1016/j.ces.2004.02.006>
- [26] Davis, S. H., and Hocking, L. M., 1999, "Spreading and imbibition of viscous liquid on a porous base," *Physics of fluids*, 11(1), pp. 48-57. <https://doi.org/10.1063/1.870416>
- [27] Starov, V., Kostvintsev, S., Sobolev, V., Velarde, M., and Zhdanov, S., 2002, "Spreading of liquid drops over dry porous layers: Complete wetting case," *Journal of Colloid and Interface Science*, 252(2), pp. 397-408. <https://doi.org/10.1006/jcis.2002.8450>
- [28] Zdražil, A., Stepanek, F., and Matar, O. K., 2006, "Droplet spreading, imbibition and solidification on porous media," *Journal of Fluid Mechanics*, 562, pp. 1-33. <https://doi.org/10.1017/S0022112006000875>
- [29] Clarke, A., Blake, T., Carruthers, K., and Woodward, A., 2002, "Spreading and imbibition of liquid droplets on porous surfaces," *Langmuir*, 18(8), pp. 2980-2984. <https://doi.org/10.1021/la0117810>
- [30] Hilpert, M., and Ben-David, A., 2009, "Infiltration of liquid droplets into porous media: Effects of dynamic contact angle and contact angle hysteresis," *International Journal of Multiphase Flow*, 35(3), pp. 205-218. <https://doi.org/10.1016/j.ijmultiphaseflow.2008.11.007>
- [31] Espín, L., and Kumar, S., 2015, "Droplet spreading and absorption on rough, permeable substrates," *Journal of Fluid Mechanics*, 784, pp. 465-486. <https://doi.org/10.1017/jfm.2015.603>
- [32] Wang, Z., Espín, L., Bates, F. S., Kumar, S., and Macosko, C. W., 2016, "Water droplet spreading and imbibition on superhydrophilic poly(butylene terephthalate) melt-blown fiber

mats," Chemical Engineering Science, 146, pp. 104-114.
<https://doi.org/10.1016/j.ces.2016.02.006>

[33] Churaev, N. V., and Sobolev, V. D., 1995, "Prediction of contact angles on the basis of the Frumkin-Derjaguin approach," Advances in Colloid and Interface Science, 61, pp. 1-16.
[https://doi.org/10.1016/0001-8686\(95\)00257-Q](https://doi.org/10.1016/0001-8686(95)00257-Q)

[34] Starov, V. M., Velarde, M. G., and Radke, C. J., 2007, Wetting and spreading dynamics, CRC press.

[35] Kumar, S. M., and Deshpande, A. P., 2006, "Dynamics of drop spreading on fibrous porous media," Colloids and Surfaces A: Physicochemical and Engineering Aspects, 277(1), pp. 157-163.
<https://doi.org/10.1016/j.colsurfa.2005.11.056>

[36] Ahmed, G., and Sellier, M., 2016, "Modeling the effects of absorption on spreading dynamics," Transport in Porous Media, 112(3), pp. 637-663. <https://doi.org/10.1007/s11242-016-0668-0>

[37] Chen, C.-Y., 2018, "Droplet Spreading on a Substrate," Master of Science, Purdue University, West Lafayette, Indiana.

[38] Barić, E., and Steiner, H., 2015, "Flow and heat transfer of non-Newtonian fluids in enameling dies," Chemical Engineering Science, 129, pp. 135-144. <https://doi.org/10.1016/j.ces.2015.02.040>

[39] Dai, Q., Khonsari, M. M., Shen, C., Huang, W., and Wang, X., 2017, "On the migration of a droplet on an incline," Journal of Colloid and Interface Science, 494, pp. 8-14.
<https://doi.org/10.1016/j.jcis.2017.01.055>

[40] Pham, T., and Kumar, S., 2019, "Imbibition and evaporation of droplets of colloidal suspensions on permeable substrates," Physical Review Fluids, 4(3), pp. 034004.
<https://doi.org/10.1103/PhysRevFluids.4.034004>

[41] Munuhe, T., Zhu, L., and Ma, R., 2021, "Thermal Analysis of CMAS Infiltration Dynamics in Thermal Barrier Coatings," Journal of Thermophysics and Heat Transfer, 35(3), pp. 611-622.
<https://doi.org/10.2514/1.T6171>

[42] Chaussonnet, G., Bravo, L., Flatau, A., Koch, R., and Bauer, H.-J., 2020, "Smoothed Particle Hydrodynamics Simulation of High Velocity Impact Dynamics of Molten Sand Particles," Energies, 13(19), pp. 5134. <https://doi.org/10.3390/en13195134>

- [43] Wiesner, V. L., and Bansal, N. P., 2015, "Mechanical and thermal properties of calcium–magnesium aluminosilicate (CMAS) glass," *Journal of the European Ceramic Society*, 35(10), pp. 2907-2914. <https://doi.org/10.1016/j.jeurceramsoc.2015.03.032>
- [44] Schwartz, L. W., and Eley, R. R., 1998, "Simulation of droplet motion on low-energy and heterogeneous surfaces," *Journal of Colloid and Interface Science*, 202(1), pp. 173-188. <https://doi.org/10.1006/JCIS.1998.5448>
- [45] Popescu, M. N., Oshanin, G., Dietrich, S., and Cazabat, A. M., 2012, "Precursor films in wetting phenomena," *Journal of Physics: Condensed Matter*, 24(24), p. 243102. <https://doi.org/10.1088/0953-8984/24/24/243102>
- [46] Dvorkin, J., 2009, "Kozeny-Carman Equation Revisited," Unpublished Paper, https://pangea.stanford.edu/~jack/KC_2009_JD.pdf
- [47] Tamayol, A., and Bahrami, M., 2011, "Transverse permeability of fibrous porous media," *Physical Review E*, 83(4), p. 046314. <https://doi.org/10.1103/PhysRevE.83.046314>
- [48] Giordano, D., Russell, J. K., and Dingwell, D. B., 2008, "Viscosity of magmatic liquids: a model," *Earth and Planetary Science Letters*, 271(1-4), pp. 123-134. <https://doi.org/10.1016/j.epsl.2008.03.038>
- [49] Kakuda, T. R., Levi, C. G., and Bennett, T. D., 2015, "The thermal behavior of CMAS-infiltrated thermal barrier coatings," *Surface and Coatings Technology*, 272, pp. 350-356. <https://doi.org/10.1016/j.surfcoat.2015.03.043>
- [50] Zhao, H., Levi, C. G., and Wadley, H. N., 2014, "Molten silicate interactions with thermal barrier coatings," *Surface and Coatings Technology*, 251, pp. 74-86. <https://doi.org/10.1016/j.surfcoat.2014.04.007>
- [51] Bisson, J. F., Fournier, D., Poulain, M., Lavigne, O., and Mévrel, R., 2000, "Thermal conductivity of yttria–zirconia single crystals, determined with spatially resolved infrared thermography," *Journal of the American Ceramic Society*, 83(8), pp. 1993-1998. <https://doi.org/10.1111/j.1151-2916.2000.tb01502.x>
- [52] Renteria, A. F., Saruhan, B., Schulz, U., Raetzer-Scheibe, H.-J., Haug, J., and Wiedenmann, A., 2006, "Effect of morphology on thermal conductivity of EB-PVD PYSZ TBCs," *Surface and Coatings Technology*, 201(6), pp. 2611-2620. <https://doi.org/10.1016/j.surfcoat.2006.05.003>

[53] Rayleigh, L., 1892, "LVI. On the influence of obstacles arranged in rectangular order upon the properties of a medium," The London, Edinburgh, and Dublin Philosophical Magazine and Journal of Science, 34(211), pp. 481-502.

Appendix A: Derivation of One-Dimensional Heat Transfer

Figure 13 shows a control volume of a spreading droplet. The energy balance at the control volume can be expressed as

$$d\dot{E}_{st} = dq_r - dq_{r+\Delta r} - dq_b + dq_s \quad (34)$$

where $d\dot{E}_{st}$ is the change rate of energy storage in the control volume, which is $(\rho c_p)_l \frac{dT_l}{dt} dV$, dq_r and $dq_{r+\Delta r}$ represent heat transfer across the radial boundaries, and dq_b and dq_s represent heat transfer across the bottom and top surfaces of the control volume, respectively. T_l represents the temperature in the liquid.

The radial heat transfer rates q_r and $q_{r+\Delta r}$ consider conduction and convection, which are expressed as:

$$\begin{aligned} dq_r &= -\left(k_l A_c \frac{dT_l}{dr}\right)_r + (\rho c_p u_l A_c dT_l)_r \\ dq_{r+\Delta r} &= -\left(k_l A_c \frac{dT_l}{dr}\right)_{r+\Delta r} + (\rho c_p u_l A_c dT_l)_{r+\Delta r} \end{aligned} \quad (35)$$

where k is thermal conductivity, $A_c = 2\pi r h$ is the radial cross-sectional area, and c_p is the specific heat of the CMAS. At the top surface, q_s is a heat flux incident on the droplet resulting from heat exchange with the high temperature environment. We can apply this as:

$$dq_s = q_s'' dA_s \quad (36)$$

Heat exchanged between the control volume and the TBC substrate is represented by dq_b . The TBC is porous so that the droplet loses heat through liquid advection as well as conduction. We can model the heat transfer through the bottom of the droplet using:

$$dq_b = -k_{eff} \frac{\partial T_p}{\partial z} \Big|_{z=0} dA_s - \rho c_p (-w_p|_{z=0}) dA_s T_l \quad (37)$$

where the bottom surface area $dA_s = 2\pi r dr$. After substituting the expressions of dq_r , $qd_{r+\Delta r}$, dq_b , and dq_s into the energy balance equation and reorganizing, we obtain the equation:

$$\begin{aligned} \frac{\partial(\rho_l c_{p,l} h T_l)}{\partial t} + \frac{1}{r} \frac{\partial}{\partial r} (\rho_l c_{p,l} u_l r h T_l) \\ = \frac{1}{r} \frac{\partial}{\partial r} \left(r h k_l \frac{\partial T_l}{\partial r} \right) + q_s'' + k_{eff} \frac{\partial T_p}{\partial z} \Big|_{z=0} - \rho_l c_{p,l} T_l w_p \Big|_{z=0} \end{aligned} \quad (38)$$

at $0 < r < R_c$

Appendix B: Validation

B.1 Droplet Spreading on an Impermeable Surface, Partial Wetting

Contact angle control is explored for a high-surface tension droplet spreading over a smooth impermeable substrate. Material properties are described in Table 6 and the initial condition is given by Eq. (15). Gravity is neglected so surface tension and wetting forces are dominant over viscosity ($Oh \ll 1$).

Droplet profiles at times $t = 0$ and $t = 50$ s are compared in Figure 14 for a partial wetting case with given equilibrium contact angle $\theta_e = 23^\circ$. At this time, the partially wetting cases have reached their steady-state solution. Equilibrium contact angles derived from solving Eq. (15) are compared against the given E values entered into Eq. (12) in Table 7. There is close agreement at the lower partial wetting contact angles.

Figure 15 compares the droplet spreading radius and center droplet height, respectively, with time and shows that it follows the expected power law behavior. Deviation at the initial stage results from the given shape of the droplet. As the droplet reaches its equilibrium contact angle, deviation from the power-law behavior occurs and is reflected in the model.

B.2 Uniform Film Infiltration in a Homogeneous Domain

Infiltration considering a uniform film is validated to confirm that the lubrication theory model works with the color function method and Darcy's law to transfer mass from the droplet porous medium. The film initially has a height of 10 μm , the porous medium is initially dry, and relevant problem parameters are described in Table 8.

The lubrication theory remains the same but the outer radius boundary conditions reflect plug flow:

$$\left. \frac{\partial h}{\partial r} \right|_{r=0} = 0, \quad \left. \frac{\partial^3 h}{\partial r^3} \right|_{r=0} = 0, \quad \left. \frac{\partial h}{\partial r} \right|_{r=L_r} = 0, \quad \left. \frac{\partial^3 h}{\partial r^3} \right|_{r=L_r} = 0 \quad (39)$$

The film surface has no curvature and it is assumed that capillary forces are dominant. Therefore, the height of the film has a negligible effect on infiltration dynamics. Then, considering infiltration under isothermal conditions, the given solutions for the droplet height and infiltration depth are:

$$\begin{aligned} h(t) &= h(0) - \sqrt{-\frac{2KP_c\varepsilon}{\mu}} t \\ h_p(t) &= \sqrt{-\frac{2KP_c}{\varepsilon\mu}} t \end{aligned} \quad (40)$$

The numerical solution agrees well with the theoretical solution as shown in Figure 16.

Figures & Tables

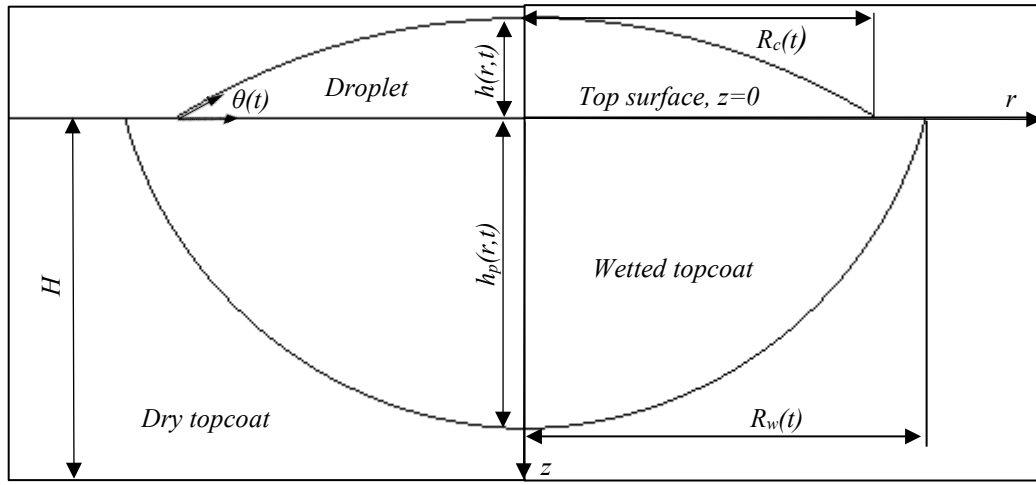


Figure 1: A partially absorbed droplet. Droplet height is magnified relative to spreading diameter.

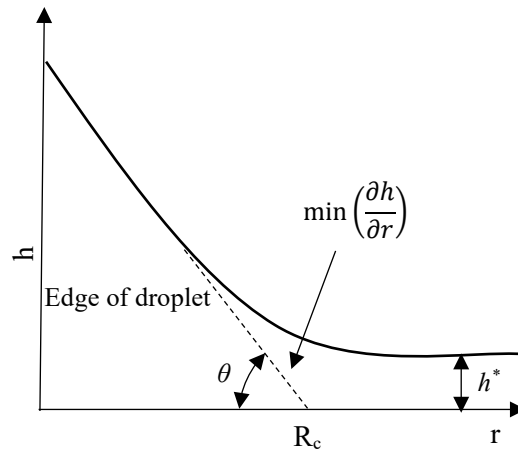


Figure 2: Contact angle and contact radius calculation during droplet spreading and recession. The precursor film thickness h^* is magnified.

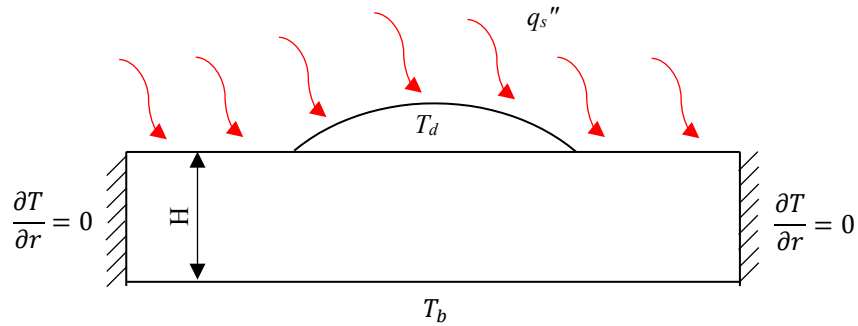


Figure 3: Thermal conditions of the topcoat

Table 1: Initial and boundary conditions for baseline case

Droplet initial contact radius	Droplet initial center height	Droplet initial temperature, T_d	Top surface heat flux, q_s''	Initial top surface temperature, based on q_s'' $T(z = 0, t = 0)$	Bottom surface temperature, T_b
71 μm	10 μm	1300°C	700 kW/m ²	1250°C	1100°C

Table 2: Material properties and simulation parameters

Variable	Symbol	Value
CMAS density	ρ_l	2690 kg/m ³ [5]
CMAS* dynamic viscosity	μ	1.6 – 24.7 Pa·s over a temperature range of 1200°C to 1400°C
Parameters in Giordano's viscosity model for sand-derived CMAS	$[A, B, C]$	-4.55, 4708, 680.8
CMAS thermal conductivity	k_f	3 W/(m·K) [14]
Molten CMAS heat capacity	$C_{p,L}$	900 J/(kg·K) (at 70°C) [47]
Molten CMAS surface tension	σ	0.4 Pa·m [48]
YSZ thermal conductivity	k_m	2.6 W/(m·K) [49]
YSZ heat capacity	$C_{p,M}$	475 J/(kg·K) (at 70°C) [47]
YSZ porous topcoat Thermal conductivity	k_{eff}	1.4 W/(m·K) (Unsaturated) [50] 2.7 W/(m·K) (Saturated) (Rayleigh equation) [53]
YSZ topcoat porosity	ε	0.15
YSZ topcoat thickness	H	300 μm
Computational domain radius	L	120 μm
Tortuosity	τ	7
Equilibrium contact angle	θ_e	13°

**Note: CMAS in this study, unless specified, refers to 33CaO-9MgO-13AlO_{1.5}-45SiO₂ with the numbers preceding the oxides denoting the mole percentage. This is a commonly studied turbine deposit of sand particles from aero-engines operating in desert environment [4, 7, 18, 43, 50].*

Table 3: Structural and transport properties of topcoat for baseline case ($K_{rr} = K_{zz}/10$)

Variable	Symbol	Value
Column characteristic length	D_i	12.7 μm
Outer diameter of annular gap	D_o	14.4 μm
Vertical permeability	K_{zz}	1.829E-16 m^2
Effective capillary radius	r_c	0.847 μm
Capillary pressure	P_c	-920.8 kPa

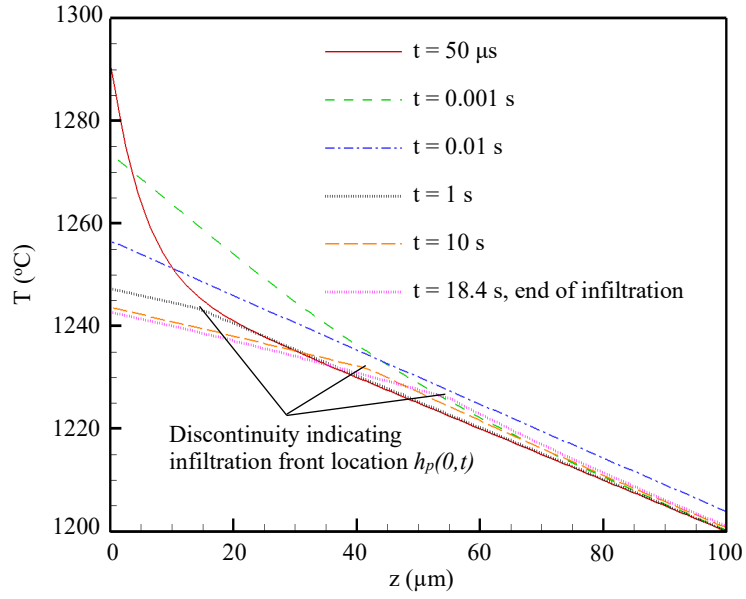


Figure 4: Vertical temperature distributions at $r=0$ in topcoat ($K_{rr} = K_{zz}/10$) at different times. Discontinuities in the temperature gradient indicate the location of the wetting front.

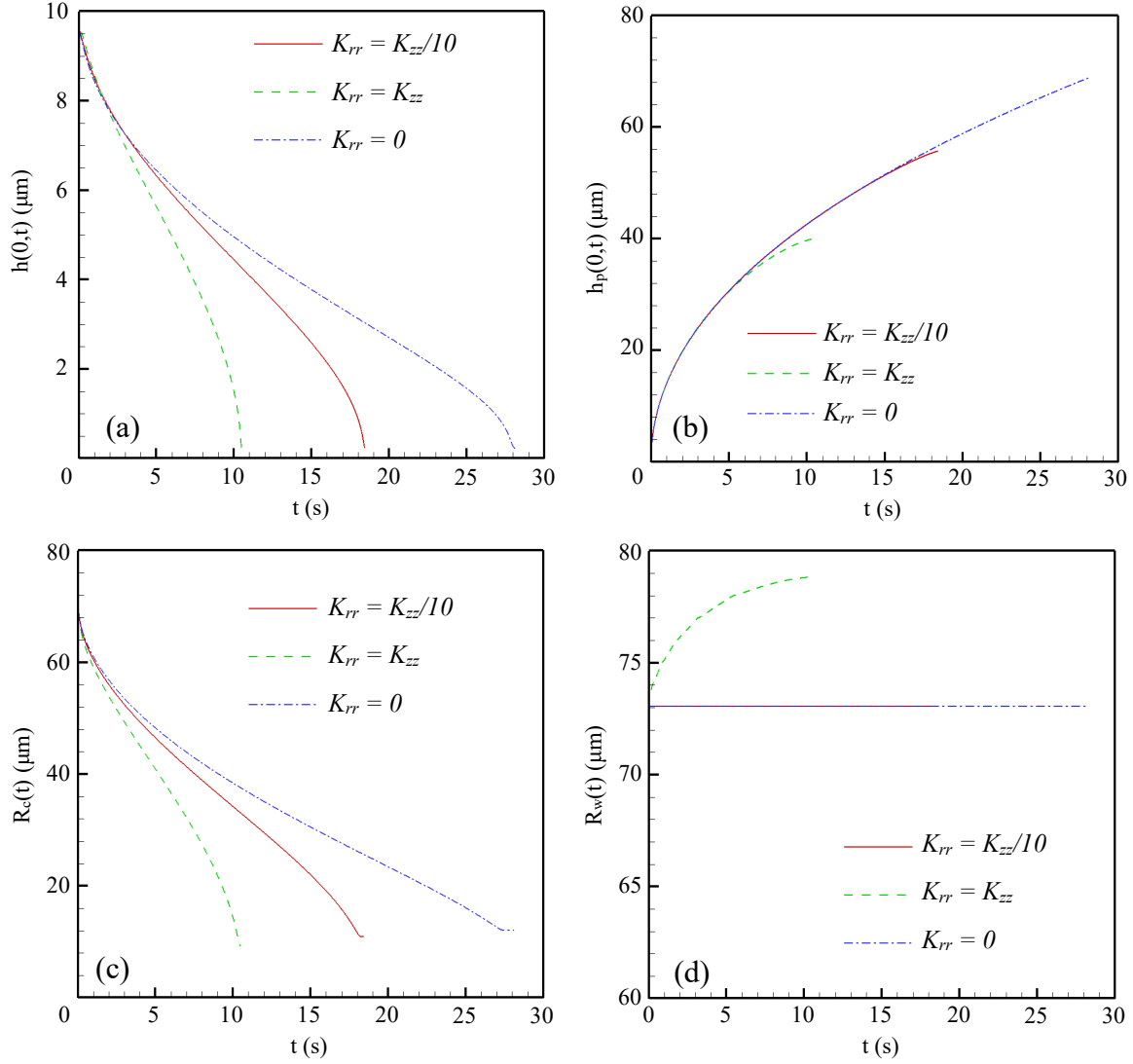


Figure 5: Spreading and infiltration dynamics considering porous media with differing anisotropy ratios: (a) droplet height $h(0,t)$, (b) infiltration depth $h_p(0,t)$, (c) contact radius $R_c(t)$, and (d) wetted radius $R_w(t)$.

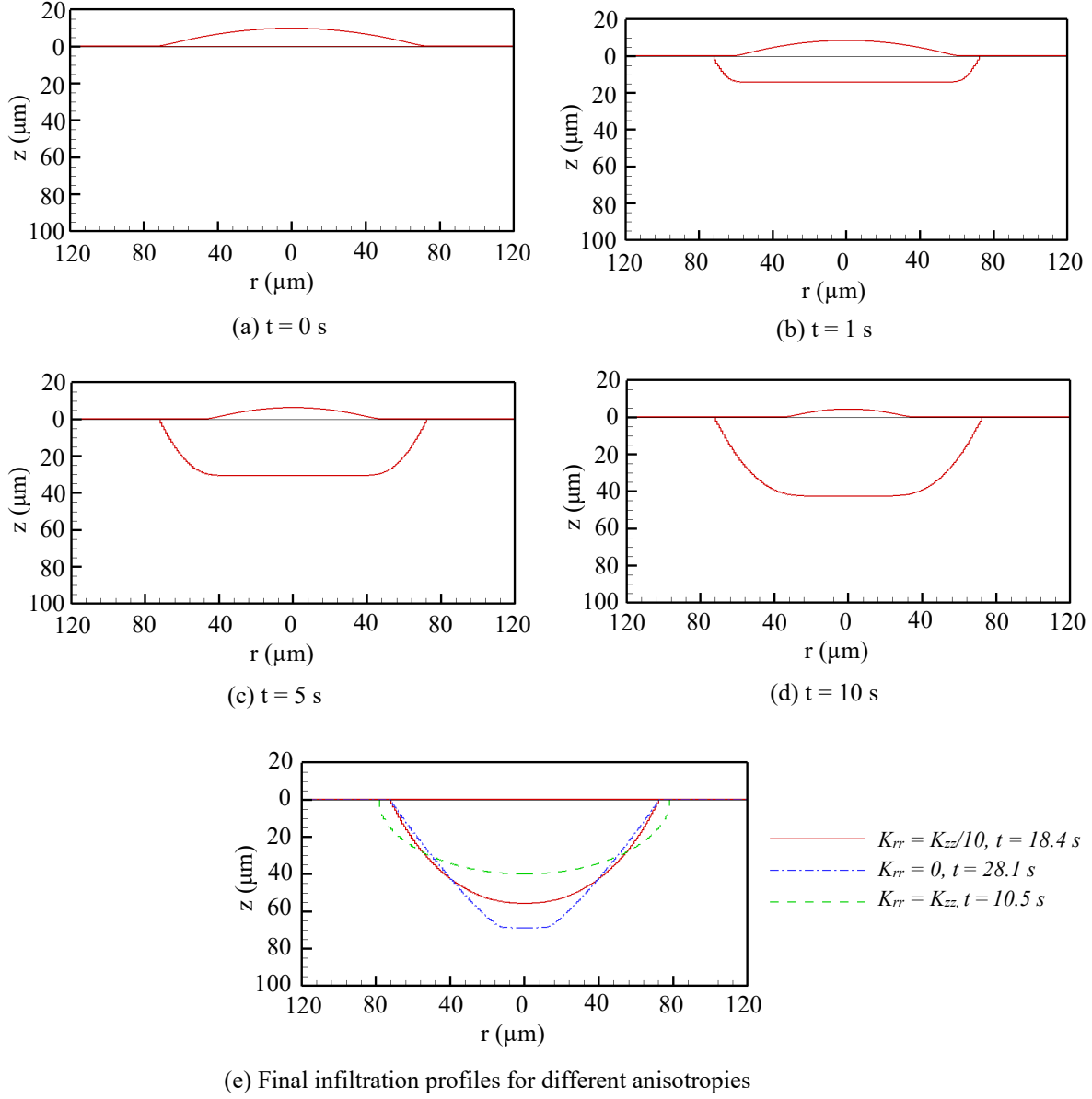


Figure 6: Evolution of droplet infiltration process in the topcoat ($K_{rr} = K_{zz}/10$) (a) initial condition at $t = 0 \text{ s}$, (b) $t = 1 \text{ s}$, (c) $t = 5 \text{ s}$, (d) $t = 10 \text{ s}$; (e) A comparison of the final infiltration profiles of the three different topcoat anisotropies.

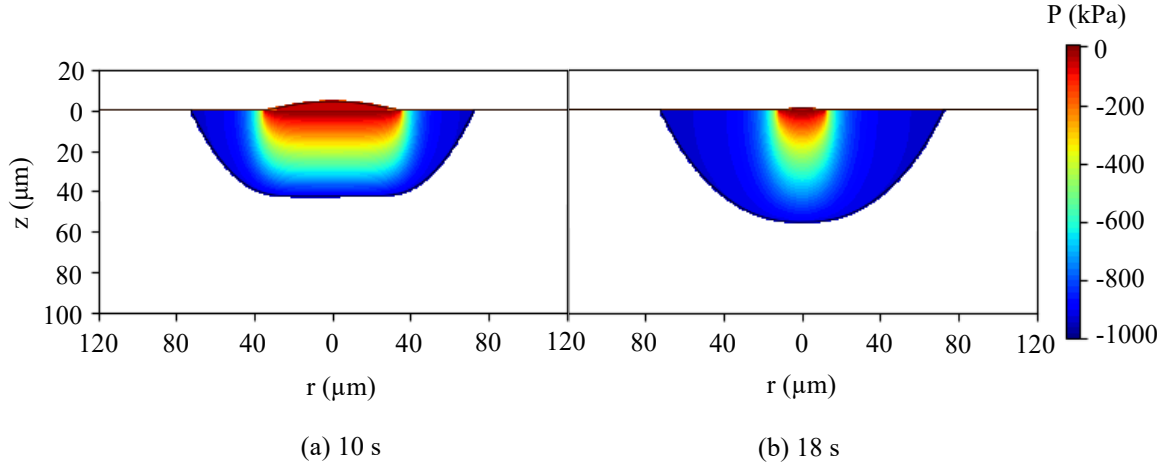


Figure 7: Pressure distributions of the base anisotropic case $K_{rr} = K_{zz}/10$ at (a) $t = 10$ s and (b) $t = 18$ s.

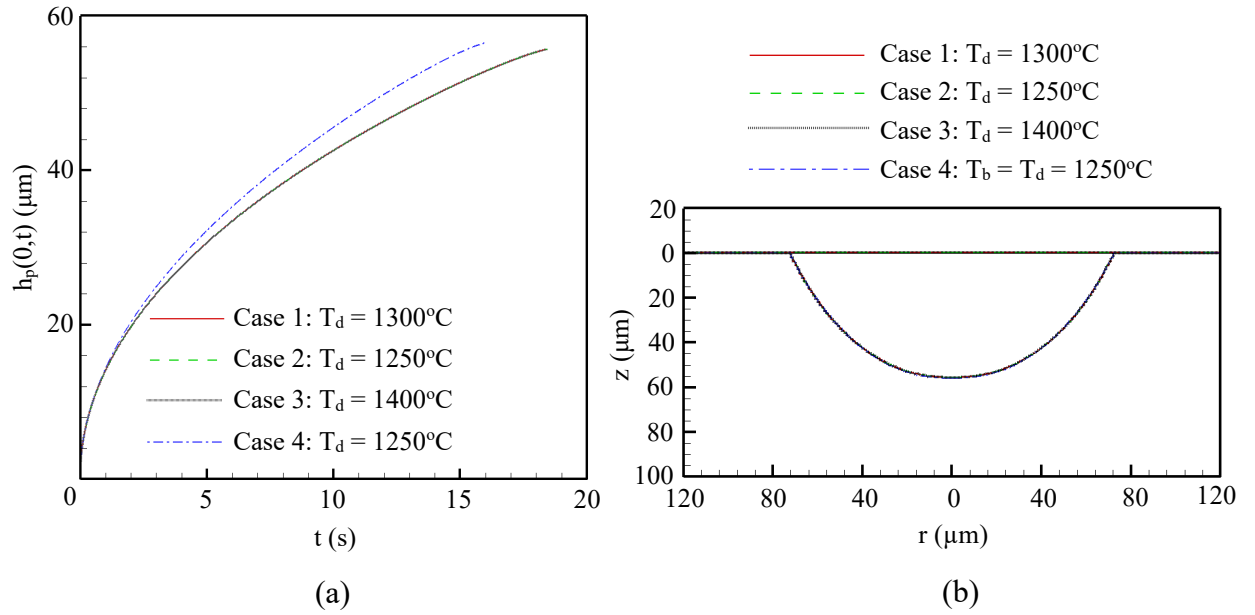


Figure 8: (a) Transient infiltration depth and (b) comparison of final infiltration profiles considering differing thermal conditions in topcoat with $K_{rr} = K_{zz}/10$.

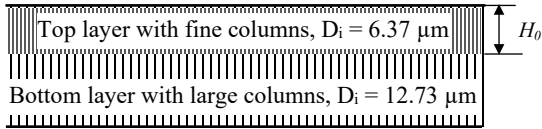
Table 1: Droplet initial temperature and topcoat thermal conditions ($K_{rr} = K_{zz}/10$)

	T_d (°C)	μ_d (Pa·s)	q_s'' (W/m ²)	T_b (°C)
Case 1	1250	10.91	700	1100
Case 2	1300	5.31	700	1100
Case 3	1400	1.56	700	1100
Case 4	1250	10.91	N/A*	1250

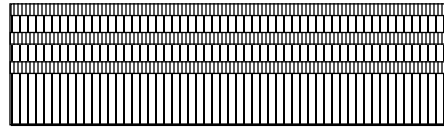
*Due to the isothermal condition in Case 4, no heat flux is applied and the topcoat is isothermal at 1250°C.

Table 5: Properties of topcoats with fine and coarse columns ($\varepsilon = 0.15$, $K_{rr} = K_{zz}/10$)

	D_o (μm)	D_i (μm)	r_c (μm)	K_{zz} (m ²)	P_c (kPa)
Coarse column	14.4	12.7	0.85	1.829E-16	-920.8
Fine column	7.2	6.4	0.42	4.571E-17	-1841.6



(a) Bilayer structure, $H_0 = 30$ μm



(b) Multilayer structure with three fine-column layers, each 10 μm in thickness and 10 μm apart

Figure 9: (a) Bilayer and (b) multilayer topcoats. Both structures have total fine structure with thickness of 30 μm, total topcoat thickness of 300 μm, and $K_{rr} = K_{zz}/10$

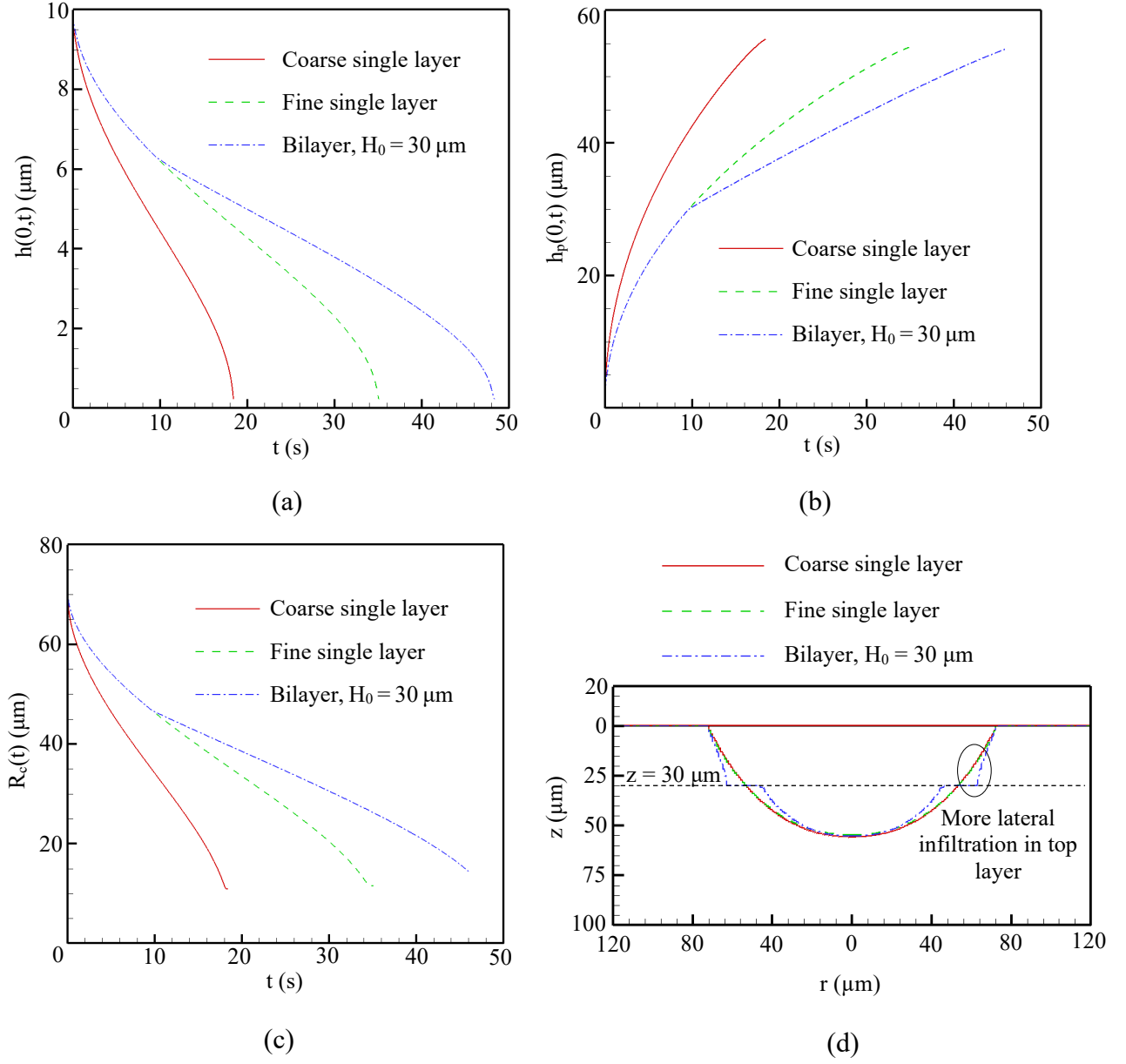


Figure 10: (a) Transient liquid droplet height $h(0,t)$, (b) infiltration depth $h_p(0,t)$, (c) contact radii $R_c(t)$, and (d) final infiltration profiles in single-layers and bilayer, $K_{rr} = K_{zz}/10$. Properties for cases described in Table 5 and Figure 9.

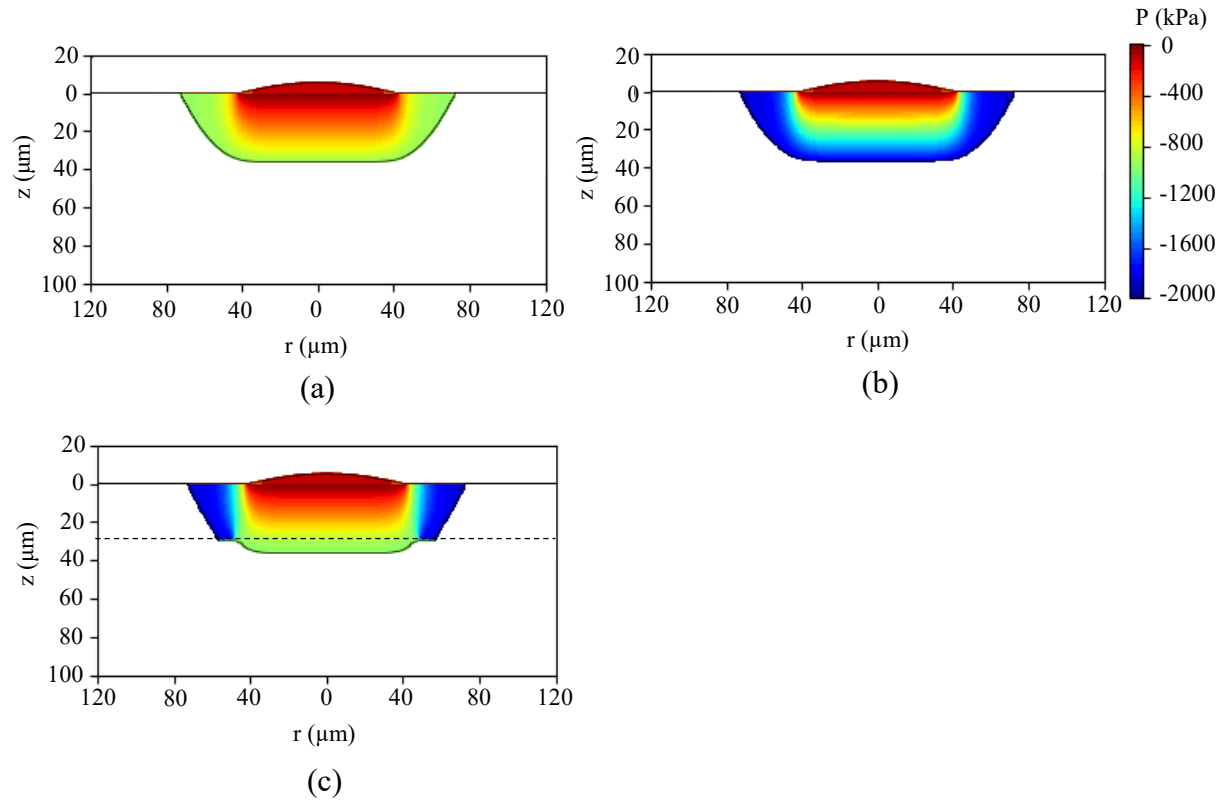
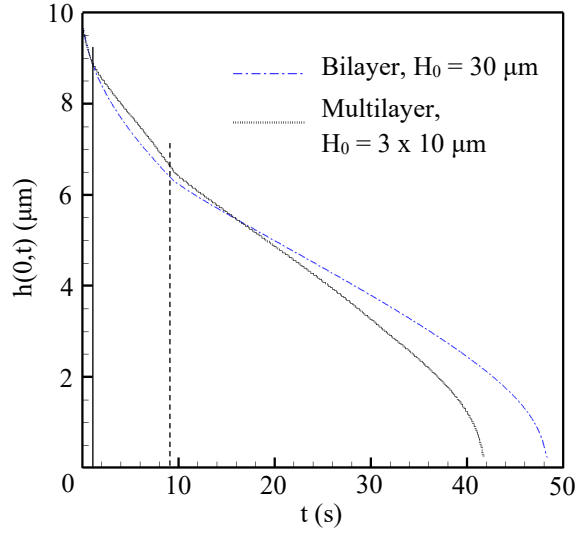
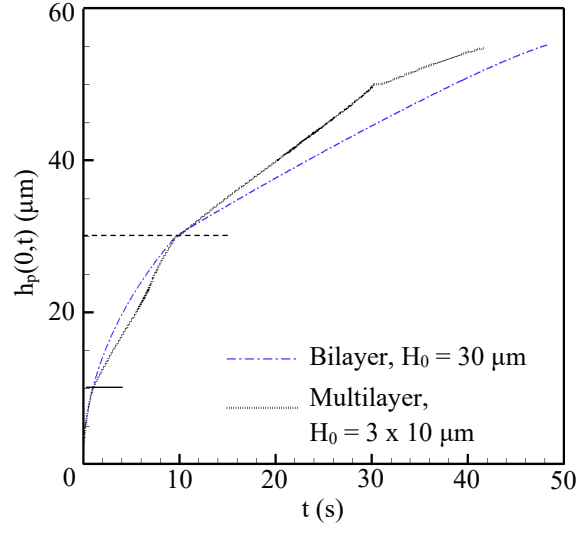


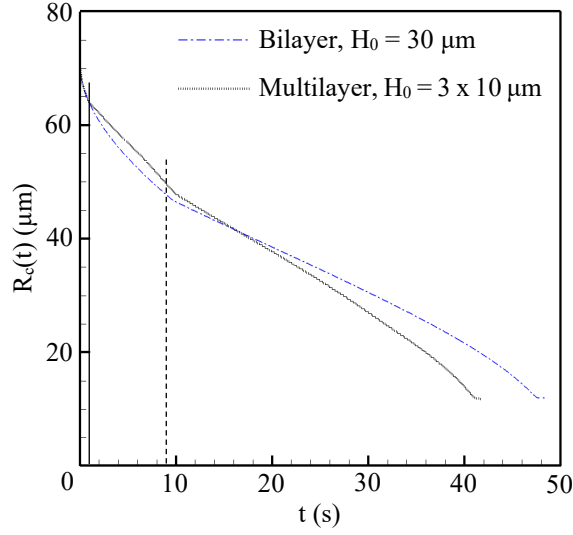
Figure 11: Pressure profile for (a) coarse single layer, (b) fine single layer, and (c) bilayer when the infiltration front reaches to $36 \mu\text{m}$ depth, $K_{rr} = K_{zz}/10$.



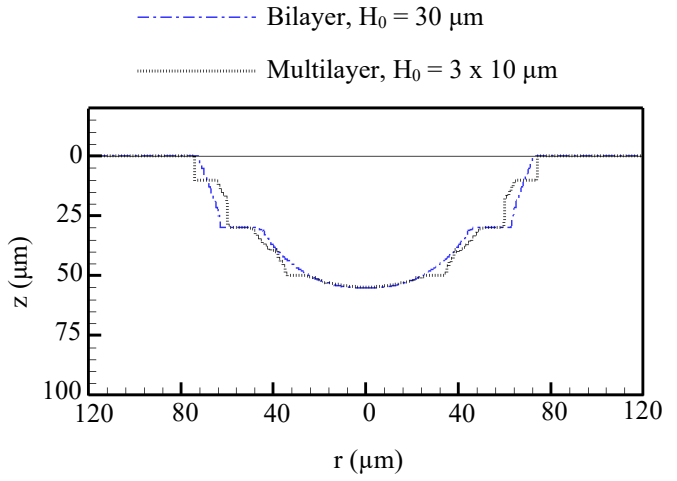
(a)



(b)



(c)



(d)

Figure 12: (a) Transient liquid droplet height $h(0,t)$, (b) infiltration depth $h_p(0,t)$, (c) contact radius $R_c(t)$, and (d) final infiltration profiles considering bilayer and multilayer porous media with the same total fine microstructure thickness ($30\text{ }\mu\text{m}$), $K_{rr} = K_{zz}/10$.

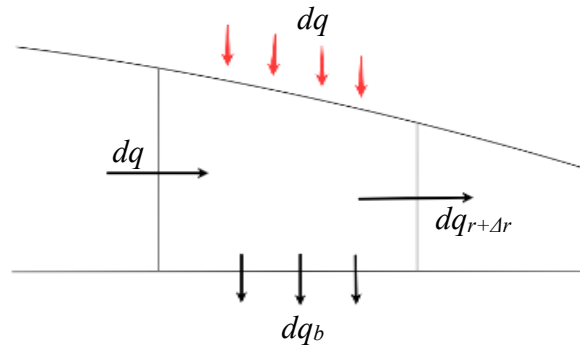


Figure 13: Differential volume of spreading droplet. The top surface is exposed to the heating from hot gases. The bottom is in contact with the porous medium and loses volume during infiltration.

Table 6: Droplet spreading parameters

Variable	Symbol	Value
Droplet Volume	V	0.5236 mL
Dynamic Viscosity	μ	0.001 Pa·s
Surface Tension	σ	0.01 Pa·m
Contact Angle	θ	0, 8, 15, 23°
Film Thickness	h^*	5E-6 m
Disjoining pressure constants	n_{Π}, m_{Π}	3, 2
Time Step	Δt	1E-5 s
Mesh size	Δr	5E-6 m

Table 7: E value in Eq. (12) vs. contact angles at $t = 50$ s. Partial wetting cases have reached equilibrium.

E	0	8.77	24.37	54.83
θ (°)	3.1	8	15	23

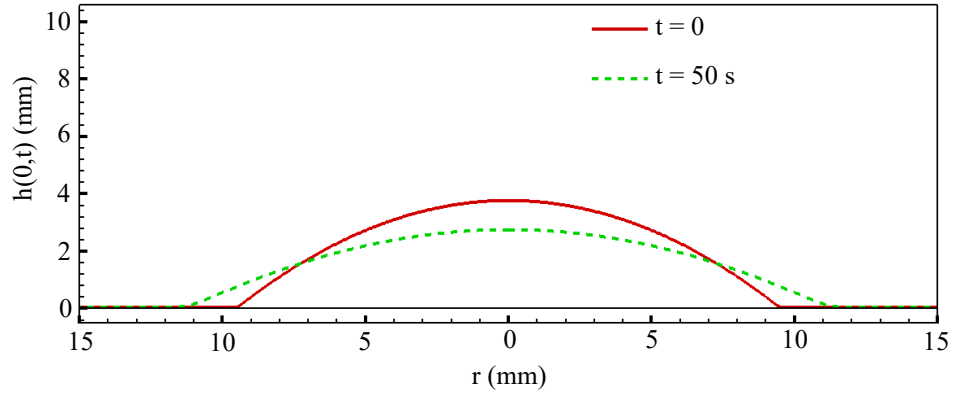
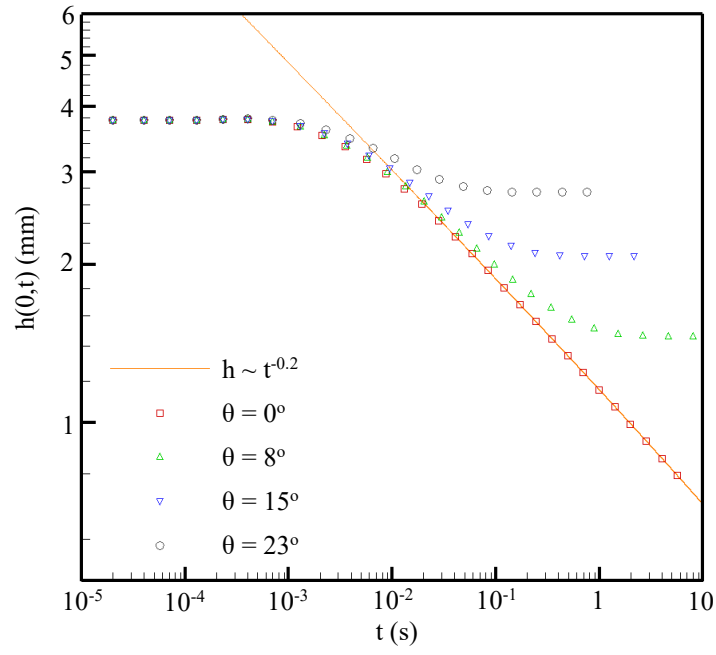
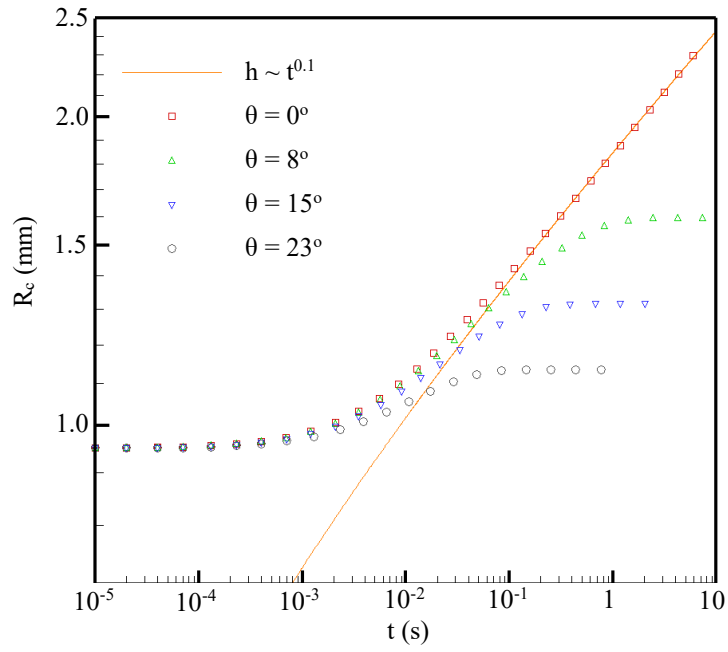


Figure 14: Comparison of initial and steady-state profile for droplet with given contact angle $\theta = 23^\circ$.



(a)



(b)

Figure 15: Comparison of droplet dynamics with different equilibrium contact angles, (a) droplet height and (b) contact radius.

Table 8: Properties for uniform
film infiltration case

μ	11 Pa·s
P_c	-945 kPa
ε	0.15
K_{zz}	9E-17 m ²
Δt	50 μ s
Δz	1 μ m

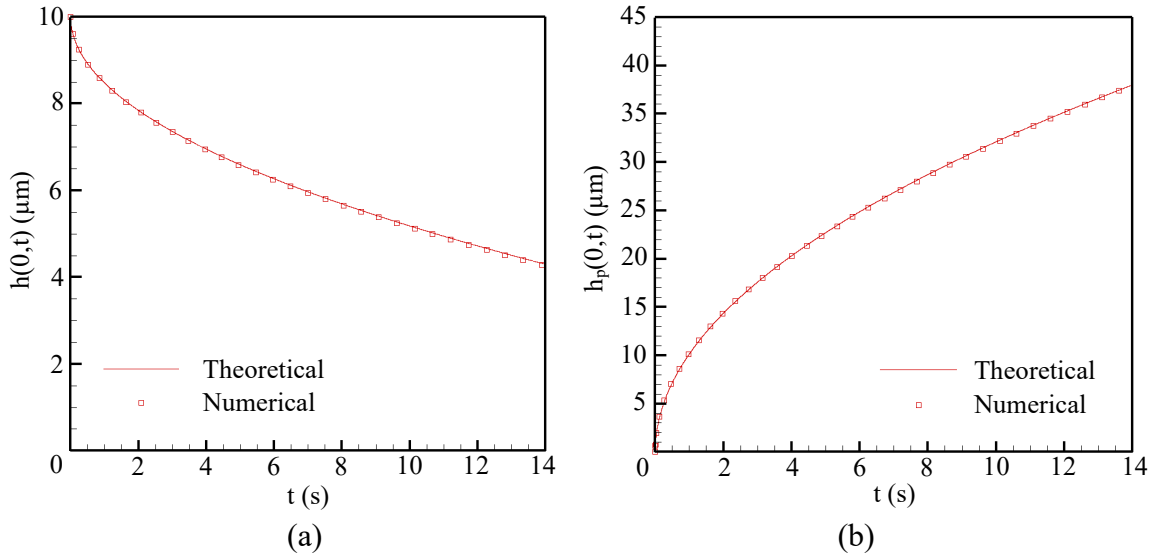


Figure 16: (a) Dynamic film thickness and (b) infiltration depth considering CMAS infiltration under isothermal conditions.